DEEP MMT[*] TRANSIT SURVEY OF THE OPEN CLUSTER M37 IV: LIMIT ON THE FRACTION OF STARS WITH PLANETS AS SMALL AS $0.3R_J$

J. D. HARTMAN[1], B. S. GAUDI[2], M. J. HOLMAN[1], B. A. MCLEOD[1], K. Z. STANEK[2], J. A. BARRANCO[3], M. H. PINSONNEAULT[2], S. MEIBOM[1], AND J. S. KALIRAI[4,5]

[1] Harvard-Smithsonian Center for Astrophysics, 60 Garden St., Cambridge, MA 02138, USA; jhartman@cfa.harvard.edu, mholman@cfa.harvard.edu, bmcleod@cfa.harvard.edu, smeibom@cfa.harvard.edu
[2] Department of Astronomy, The Ohio State University, Columbus, OH 43210, USA; gaudi@astronomy.ohio-state.edu, pinsono@astronomy.ohio-state.edu, kstanek@astronomy.ohio-state.edu
[3] Department of Physics and Astronomy, San Francisco State University, 1600 Holloway Ave., San Francisco, CA 94132, USA; barranco@stars.sfsu.edu
[4] University of California Observatories/Lick Observatory, University of California at Santa Cruz, Santa Cruz, CA 95060, USA; jkalirai@ucolick.org

ABSTRACT

We present the results of a deep ($15 \lesssim r \lesssim 23$), 20 night survey for transiting planets in the intermediate-age open cluster M37 (NGC 2099) using the Megacam wide-field mosaic CCD camera on the 6.5 m MMT. We do not detect any transiting planets among the $\sim$1450 observed cluster members. We do, however, identify a $\sim 1R_J$ candidate planet transiting a $\sim 0.8\ M_\odot$ Galactic field star with a period of 0.77 days. The source is faint ($V = 19.85$ mag) and has an expected velocity semiamplitude of $K \sim 220$ m s^{-1} (M/M_J). We conduct Monte Carlo transit injection and recovery simulations to calculate the 95% confidence upper limit on the fraction of cluster members and field stars with planets as a function of planetary radius and orbital period. Assuming a uniform logarithmic distribution in the orbital period, we find that $<1.1\%$, $<2.7\%$, and $<8.3\%$ of cluster members have $1.0R_J$ planets within extremely hot Jupiter (EHJ; $0.4 < P < 1.0$ day), very hot Jupiter (VHJ; $1.0 < P < 3.0$ day), and hot Jupiter (HJ; $3.0 < P < 5.0$ day) period ranges, respectively. For $0.5R_J$ planets, the limits are less than 3.2% and less than 21% for EHJ and VHJ period ranges, respectively, while for $0.35R_J$ planets we can only place an upper limit of less than 25% on the EHJ period range. For a sample of 7814 Galactic field stars, consisting primarily of FGKM dwarfs, we place 95% upper limits of $<0.3\%$, $<0.8\%$, and $<2.7\%$ on the fraction of stars with a $1.0R_J$ EHJ, VHJ, and HJ, respectively, assuming that the candidate planet is not genuine. If the candidate is genuine, the frequency of $\sim 1.0R_J$ planets in the EHJ period range is $0.002\% < f_{\rm EHJ} < 0.5\%$ with 95% confidence. We place limits of $<1.4\%$, $<8.8\%$, and $<47\%$ for $0.5R_J$ planets, and a limit of $<16\%$ on $0.3R_J$ planets in the EHJ period range. This is the first transit survey to place limits on the fraction of stars with planets as small as Neptune.

Key words: open clusters and associations: individual (M37) – planetary systems – surveys

1. INTRODUCTION

The discovery by Mayor & Queloz (1995) of a planet with half the mass of Jupiter orbiting the solarlike star 51 Pegasi with a period of only 4.23 days shocked the astronomical community. The existence of such a "hot Jupiter" (HJ) defied the prevailing theories of planet formation, which had been tailored to explain the architecture of the solar system. Since then, radial velocity (RV) surveys for planets orbiting nearby F, G, and K main-sequence stars have determined that $1.2\% \pm 0.2\%$ of these stars host a HJ (Marcy et al. 2005, where a HJ is defined as a planet roughly the size of Jupiter that orbits within 0.1 AU of its star), with indications that this frequency depends on the metallicity of the host star (such that the frequency is roughly proportional to $10^{2[{\rm Fe/H}]}$; Fischer & Valenti 2005).

Over the last decade, there have been numerous surveys for extrasolar planets following a variety of techniques (e.g., Butler et al. 2006) with the goal of determining the planet occurrence rate in new regions of parameter space. A successful technique has been to conduct photometric searches for planets that transit their host stars. This technique is particularly sensitive to planets on close-in orbits. To date, more than 50 planets

have been discovered by this technique,[6] including numerous very hot Jupiters (VHJs) with orbital periods between one and three days. Gaudi et al. (2005) used the four transiting planets discovered at the time by the Optical Gravitational Lensing Experiment (OGLE) collaboration (Udalski et al. 2002; Konacki et al. 2003, 2004; Bouchy et al. 2004; Pont et al. 2004) to determine that only 0.1%–0.2% of FGK stars host a VHJ. Gould et al. (2006) conducted a thorough analysis of the OGLE survey to determine that the frequency of VHJs is $f_{\rm VHJ} = (1/710)(1^{+1.10}_{-0.54})$ and $f_{\rm HJ} = (1/320)(1^{+1.37}_{-0.59})$, while Fressin et al. (2007) found $f_{\rm VHJ} = (1/560)$ and $f_{\rm HJ} = (1/320)$. The Sagittarius Window Eclipsing Extrasolar Planet Search (SWEEPS) survey for transiting planets in the Galactic bulge conducted with the *Hubble Space Telescope* (*HST*) (Sahu et al. 2006) identified a putative class of ultrashort-period planets or extremely hot Jupiters (EHJs) with periods less than one day orbiting stars lighter than $0.88\ M_\odot$. They concluded that $\sim$0.4% of bulge stars more massive than $\sim 0.44\ M_\odot$ are orbited by a Jupiter-sized planet with a period less than 4.2 days, though they estimated that this fraction is uncertain by a factor of 2. Note that due to their faintness, the majority of the SWEEPS candidates are unconfirmed with RV follow up. In addition to these two surveys, the Trans-Atlantic Exoplanet Survey (TrES) (e.g, Alonso et al. 2004), Hungarian-made Automatic

---

6 http://exoplanet.eu

Telescope Network (HATNet) (e.g., Bakos et al. 2007), XO (e.g., McCullough et al. 2006), and Wide Area Search for Planets (WASP) (e.g., Collier-Cameron et al. 2007) surveys have all discovered planets orbiting relatively bright stars in the Galactic field, though to date these surveys have not been used to calculate the planet occurrence frequency.

While photometric surveys of Galactic field stars have been quite successful at finding transiting planets over the last few years, it is generally difficult to measure the planet occurrence frequency with these surveys (for discussions of how this can be done despite the difficulties, see Gould et al. 2006; Fressin et al. 2007; Gaudi 2007; Beatty & Gaudi 2008). The difficulty arises from the uncertainty in the parameters (mass, radius, metallicity) of the surveyed stars. Moreover, typical field surveys yield numerous false positives that are often culled in part by eye; these culling procedures are generally difficult to model in determining the detection efficiency of the survey. In contrast to field surveys, surveys of globular and open star clusters observe a population of stars with parameters that are relatively easy to determine en masse; moreover, many of the false positive scenarios are less common for this type of survey. Significant work has been invested in developing optimum strategies to search for planets in stellar clusters (Janes 1996; von Braun et al. 2005; Pepper & Gaudi 2005). A number of groups have completed transit surveys of open clusters, including the UStAPS (Street et al. 2003; Bramich et al. 2005; Hood et al. 2005), EXPLORE-OC (von Braun et al. 2005), PISCES (Mochejska et al. 2005, 2006), STEPSS (Burke et al. 2006, hereafter B06), and MONITOR (Aigrain et al. 2007) projects, and a survey by Montalto et al. (2007). There have also been several surveys of globular clusters (Gilliland et al. 2000; Weldrake et al. 2005; Weldrake et al. 2008).

While to date no confirmed transiting planet has been found in a stellar cluster, many of these surveys have placed limits on the frequency of hot transiting planets, typically as functions of planetary radius as well as period. The globular cluster surveys have placed the most stringent constraints; the null result for the core of 47 Tucanae by Gilliland et al. (2000) suggests that the frequency of an HJ in this environment is at least an order of magnitude less than for the solar neighborhood, while the null result for the outskirts of the same cluster by Weldrake et al. (2005) is inconsistent with the planet frequency in the solar neighborhood at the 3.3σ level and suggests that the dearth of planets in this globular cluster is due to low metallicity rather than crowding effects. The open cluster surveys, on the other hand, have typically placed limits on the occurrence frequency that are well above the 1.2% measured by the RV surveys. Notably, B06 conducted a thorough Monte Carlo simulation of their transit survey of the open cluster NGC 1245 to limit the frequency of an EHJ, VHJ, and HJ with radii of $1.5R_J$ to $<1.5\%$, $<6.4\%$, and $<52\%$, respectively. The fundamental limit on the ability of open cluster surveys to place meaningful limits on the occurrence frequency of Jupiter-sized planets appears to be due to the relatively small number of stars in an open cluster. B06 found that for their survey strategy, ~7400 dwarf stars would have to be observed for at least a month to put a limit of less than 2% on the planet frequency, which is significantly larger than the typical size of an open cluster. One open cluster that has been a popular target is NGC 6791. This cluster is old ($t \sim 8$ Gyr, Carraro et al. 2006, Kalirai et al. 2007), metal rich ($[M/H] \sim +0.4$; Gratton et al. 2006; Origlia et al. 2006) and contains a large number of stars ($M > 4000\ M_\odot$; Kaluzny & Udalski 1992), though it is also very distant (($m - M)_0 \sim 12.8$;

Stetson et al. 2003) so that lower main-sequence stars in the cluster are quite faint. It has been the target of three transit searches (Bruntt et al. 2003; Mochejska et al. 2005; Montalto et al. 2007), the most recent of which found that their null result is inconsistent at the $\sim95\%$ level with the RV HJ frequency at high metallicity.

The paucity of stars in open clusters appears to limit their usefulness as probes of the HJ frequency (excluding, perhaps, the result from Montalto et al. 2007). They may, however, be useful for probing smaller planet radii (see Pepper & Gaudi 2006). In the last several years, RV surveys have discovered a number of Neptune and super-Earth-mass planets (HN, $M<0.1M_J$; Butler et al. 2004; Endl et al. 2008; Fischer et al. 2008; Lovis et al. 2006; Melo et al. 2007; Rivera et al. 2005; Santos et al. 2004; Udry et al. 2006, 2007; Vogt et al. 2005). One of these planets, GJ 436 b, has been discovered to transit its host star (Gillon et al. 2007). Little, however, is known about the frequency of these planets. Determining or placing meaningful limits on this frequency would provide a powerful test of planet formation models. The theoretical predictions of the frequency of these objects run the gamut from a steep decline in the frequency of HN relative to the HJ (Ida & Lin 2004), except perhaps for M-dwarfs (Ida & Lin 2005), to HN being ubiquitous (Brunini & Cionco 2005).

In this paper, the fourth and final in a series, we present the results of a survey for transiting hot planets as small as Neptune in the intermediate-age open cluster M37 (NGC 2099) using the MMT. We were motivated to conduct this transit survey by Pepper & Gaudi (2005, 2006), who suggested that it may be possible to find Neptune-sized planets transiting solarlike stars by surveying an open cluster with a large telescope. The Megacam mosaic imager on the MMT (McLeod et al. 2000) is an ideal facility for conducting such a survey due to its wide field of view (FOV) and deep pixel wells that oversample the stellar point-spread function (PSF). Preliminary observations of NGC 6791 suggested that finding Neptune-sized planets was indeed technically feasible using this facility (Hartman et al. 2005). Using the formalism developed by Pepper & Gaudi (2005), we found that M37 is the optimum target for MMT/Megacam to maximize the number of stars to which we would be sensitive to Neptune-sized planets. We note that a drawback of this type of survey is that any identified candidates will be quite faint making follow-up RV confirmation difficult. For planets significantly smaller than $1.0R_J$, false positives where the transiting object is a small star or brown dwarf are no longer applicable. Given the depth of the survey very few giants will be included in the sample, and those that are can easily be rejected based on their colors. Low-precision spectroscopy may be sufficient to rule out various blended binary scenarios. Therefore, it is reasonable to suppose that for a given small-radius candidate one could make a strong argument that the object is a real planet without obtaining a RV determination of its mass. Also note that similar difficulties will be faced by the *Corot* and *Kepler* space missions (albeit for even smaller planets), so our experiment may provide a useful analogy to these missions.

We conducted the survey over 20 nights between 2005 December and 2006 January, accumulating more than 4000 quality images of the cluster. This is easily the largest telescope ever utilized for such a survey. In the first paper in the series (Hartman et al. 2008a, Paper I), we describe the observations and data reduction, combine photometric and spectroscopic data to refine estimates for the cluster fundamental parameters ($t = 550 \pm 30$ Myr with overshooting, $[M/H] = +0.045 \pm 0.044$,

$(m − M)_V = 11.57 ± 0.13$ mag and $E(B − V) = 0.227 ± 0.038$ mag), and determine the cluster mass function down to 0.3 $M_⊙$. In the second paper (Hartman et al. 2008b, Paper II) we analyze the light curves of ∼23000 stars observed by this survey to discover 1430 variable stars. In the third paper (Hartman et al. 2009, Paper III), we use the light curves to measure the rotation periods of 575 probable cluster members. This is the largest sample of rotation periods for a cluster older than a few hundred Myr, and thus provides a unique window on the late time rotation evolution of low-mass main-sequence stars.

In the following section, we will summarize our observations and data reduction. In Section 3 we discuss the pipeline used to remove systematic variations from light curves and identify candidate transiting planets. In Section 4 we describe the candidate transiting planets identified by this survey, finding no candidates that are probable cluster members. In Section 5, we conduct Monte Carlo simulations to determine the transit detection efficiency of our survey. In Section 6, we present our results on the limit of stars with planets for various planetary radii and orbital periods. Finally, we conclude in Section 7.

2. SUMMARY OF OBSERVATIONS AND DATA REDUCTION

The observations and data reduction procedure were described in detail in Papers I and II; we provide a brief overview here. The photometric observations consist of *gri* photometry for ∼16, 000 stars, *gri* photometry for stars in a field located $2°$ from the primary M37 field and at the same Galactic latitude, and *r* time-series photometry for ∼23, 000 stars, all obtained with the Megacam instrument (McLeod et al. 2000) on the 6.5 m MMT. Megacam is a $24' × 24'$ mosaic imager consisting of 36 2k×4k, thinned, backside-illuminated CCDs that are each read out by two amplifiers. The mosaic has an unbinned pixel scale of 0.″08, which allows for a well-sampled PSF even under the best-seeing conditions. To decrease the read-out time, we used $2 × 2$ binning with the gain set so that the pixel sensitivity became nonlinear before the analog-to-digital conversion threshold of 65,536 counts. Because of the fine sampling and the relatively deep pixel wells, one can collect $2 × 10^7$ photons in $1''$ seeing from a single star prior to saturation, setting the photon limit on the precision in a single exposure to ∼0.25 mmag.

The primary time-series photometric observations consist of ∼4000 high quality images obtained over 24 nights (including eight half-nights) between 2005 December 21 and 2006 January 21. We obtained light curves for stars with $14.5 \lesssim r \lesssim 23$ using a reduction pipeline based on the image subtraction technique and software due to Alard & Lupton (1998) and Alard (2000). The resulting light curves were passed through the processing and transit detection pipeline that we describe in Section 3. We used the DAOPHOT 2 and ALLSTAR PSF fitting programs and the DAOGROW program (Stetson 1987, 1990, 1992) to obtain the *g*, *r*, and *i* single-epoch photometry.

As described in Paper I we also take *BV* photometry for stars in the field of this cluster from Kalirai et al. (2001), K_S photometry from the Two Micron All Sky Survey (2MASS) (Skrutskie et al. 2006), and we transform our *ri* photometry to I_C using a transformation based on the I_C photometry from Nilakshi & Sagar (2002).

In addition to the photometry, we also obtained high-resolution spectroscopy of 127 stars using the Hectochelle multifiber, high-dispersion spectrograph (Szentgyorgyi et al. 1998) on the MMT. The spectra were obtained on four separate nights between 2007 February 23 and 2007 March 12 and were used to measure $T_{\rm eff}$, [Fe/H], $v \sin i$, and the RV via crosscorrelation against a grid of model stellar spectra computed using ATLAS 9 and SYNTHE (Kurucz 1993). The classification procedure was developed by S. Meibom et al. (2009, in preparation), and made use of the *xcsao* routine in the IRAF[7] *rvsao* package (Kurtz & Mink 1998) to perform crosscorrelation. We use these spectra to provide stellar parameters and RV measurements for several of the host stars to the candidate transiting planets.

3. TRANSIT SELECTION PIPELINE

In this section, we describe the pipelines used to remove systematic variations from the light curves and select candidate transiting planets. We use these pipelines first to identify candidates (Section 4) and then to calibrate the detection efficiency by conducting transit injection and recovery simulations (Section 5). The pipeline includes several steps: postprocessing the light curves, devising transit selection criteria, and applying the selection criteria to the data to find candidates. We have devised three distinct pipelines, which we refer to as selection criteria sets 1–3, that differ in the number of postprocessing routines applied and the manner in which candidates are selected. We first discuss the postprocessing routines and the precision of the resulting postprocessed light curves; we then discuss the selection criteria.

3.1. Light-Curve Postprocessing

The raw light curves returned from the image subtraction procedure exhibit substantial scatter due to instrumental artifacts as well as astrophysical variations. Before searching these light curves for low-amplitude transit signals we must take steps to reduce the time-correlated noise. This process may reduce the sensitivity to high signal-to-noise ratio (S/N) planets, so for selection criteria set 3 we only apply a limited postprocessing routine. Our postprocessing pipeline consists of the following steps:

1. (Selection criteria sets 1–3) We first clip points from each light curve that are more than five standard deviations from the mean magnitude. We perform two iterations of this procedure.

2. (Selection criteria sets 1–3) For each image *i*, we determine f_i, the fraction of light curves for which image *i* is at least a 3σ outlier. Images with $f_i > f_c$, the cutoff fraction, are removed from all the light curves. This process is performed independently for each of the 36 chips. We choose f_c for each chip based on a visual inspection of the histogram of f_i values; we use values that range from 3% to 5%. This process typically removes ∼500 images from the light curves.

3. (Selection criteria sets 1 and 2 only) We then remove one sidereal day or 0.9972696 day period signals from the light curves. This is done to remove artifacts due to, for example, rotating diffraction spikes that have a period of exactly one sidereal day. Figure 1 shows an example of a light curve that exhibits brightenings at a period of one sidereal day as diffraction spikes from nearby bright stars sweep over the star. The diffraction spikes rotate in the image due to the need to rotate the camera with respect to the secondary

---

[7] IRAF is distributed by the National Optical Astronomy Observatory, which is operated by the Association of Universities for Research in Astronomy, Inc., under cooperative agreement with the National Science Foundation.
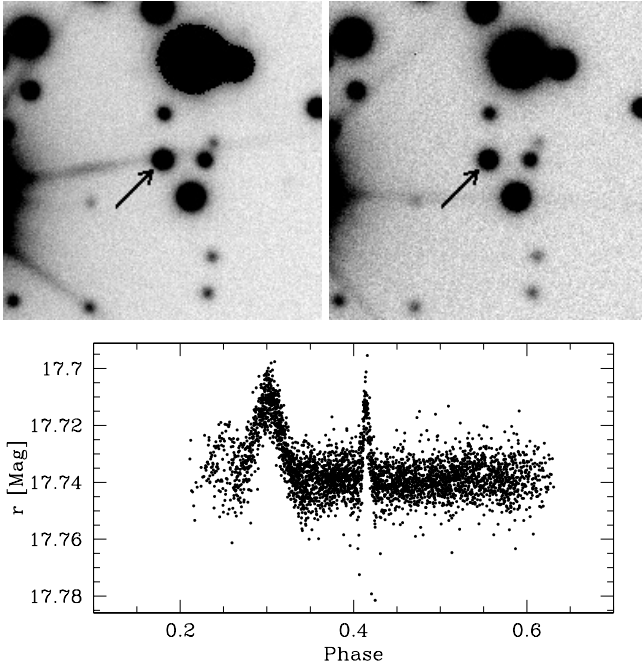
Figure 1. Example of a star with a light curve that shows repeated brightenings due to diffraction spikes from a neighboring bright star. The upper two panels show the star in question on a $0\rlap{.}''5 \times 0\rlap{.}''5$ FOV, when a diffraction spike is over the star (left) and when no spike is over the star (right). The two images were taken 100 minutes apart. The bottom panel shows the light curve of the star phased at a one sidereal day; note the two periodic brightenings caused by the rotation of diffraction spikes in the images over the course of each night.

mirror supports to keep stars on the same pixels throughout the night on the alt-az MMT. The number, width, depth, and shape of the brightenings seen in the light curves vary from star to star; moreover, additional artifacts such as color-dependent atmospheric extinction will also give rise to apparent variability with a period of one sidereal day. We remove these signals by binning the light curves in phase, using 200 bins, and then adjusting the points in a bin by an offset so that the average of the bin is equal to the average of the light curve.

4. (Selection criteria sets 1 and 2 only) As discussed in Paper III, we found that ∼1/3 of the probable cluster members that we observed show quasi-periodic variations with amplitudes of ∼1% and periods ranging from 0.3 to 15 days. These variations are due to the presence of large spots on the surfaces of these relatively young (550 Myr), rapidly rotating stars. While it may be possible to identify a ∼1% transit on top of such a signal, it would be increasingly difficult to identify shallower transits without taking steps to remove these variations. Using the Lomb–Scargle algorithm (Lomb 1976; Scargle 1982; Press & Rybicki 1989), we identify the period P of the best-fit sine curve to each light curve. We then fit to the poststep-3 light curve a signal of the form

$$m = A_0 + A_1 \sin(2Pt/2\pi + \phi_1) + A_2 \sin(Pt/2\pi + \phi_2)$$
$$+ A_3 \sin(0.5Pt/2\pi + \phi_3), \qquad (1)$$

where A_i and ϕ_i are free parameters and we calculate $\Delta\chi^2_{\mathrm{Harm}}$, the reduction in χ^2 after subtracting the best-fit model from the light curve. Note that we adopt the convention that a more negative value of $\Delta\chi^2$ indicates a better fit of the model to the data. This process increases the sensitivity to shallow transits but decreases the sensitivity to
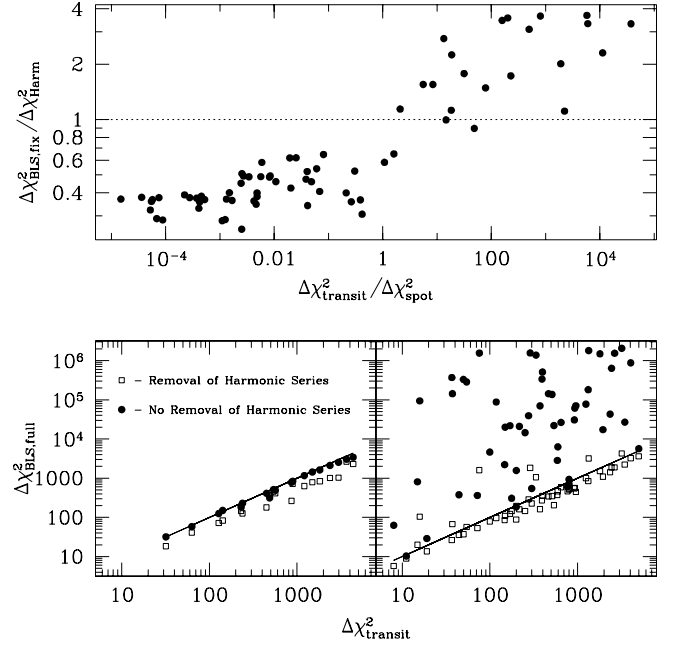

Figure 2. Transit recovery results for model light curves including both transits and photometric variations due to starspots. (Top) Comparison between the ratio of the model transit strength to the model spot strength, measured as a contribution to χ^2 for each simulated signal, and the ratio of the best boxcar fit to the best harmonic series fit at the peak $L-S$ period. We divide the data into two classes: those with $\Delta\chi^2_{\mathrm{BLS,fix}}/\Delta\chi^2_{\mathrm{Harm}} > 1$ (i.e., a transit model fits the light curve better than a spot model) and those with $\Delta\chi^2_{\mathrm{BLS,fix}}/\Delta\chi^2_{\mathrm{Harm}} < 1$ (i.e., a spot model fits the light curve better than a transit model). (Bottom) Comparison between the best-fit BLS transit model, using a full-period search, and the strength of the injected transit. We show the results separately for simulations with $\Delta\chi^2_{\mathrm{BLS,fix}}/\Delta\chi^2_{\mathrm{Harm}} > 1$ (left) and simulations with $\Delta\chi^2_{\mathrm{BLS,fix}}/\Delta\chi^2_{\mathrm{Harm}} < 1$ (right). In each plot, we show the results for both removing and not removing a best-fit harmonic series from the light curve before running the full BLS search. The solid lines show the ideal relation where $\Delta\chi^2_{\mathrm{BLS,full}} = \Delta\chi^2_{\mathrm{transit}}$. When the transit model fits the light curve better than a harmonic series (left), the harmonic series should not be removed from the light curve; when the harmonic series fits the light curve better (right), it should be removed before searching for transits.

deep transits. We therefore fit a box-car transit signal to the poststep-3 light curve, without subtracting the sine curve, phased at period P using the box-fitting least squares (BLS) algorithm (Kovács et al. 2002) and calculate $\Delta\chi^2_{\mathrm{BLS,fix}}$, the reduction in χ^2 after subtracting the box-car transit model from the light curve. We subtract Equation (1) from light curves with $\Delta\chi^2_{\mathrm{Harm}} < \Delta\chi^2_{\mathrm{BLS,fix}}$, that is, we only apply the correction to light curves for which a harmonic series fits the phased light curve better than a transit signal. To test this technique, we simulate light curves including variability due to spots as well as transits. We use the Dorren (1987) spot model and the Mandel & Agol (2002) transit model. Figure 2 compares the results of a full BLS search on light curves with deep transits relative to spots and vice versa for the two cases of removing and not removing a harmonic signal before running BLS. We see that removing a harmonic series from light curves with $\Delta\chi^2_{\mathrm{Harm}} < \Delta\chi^2_{\mathrm{BLS,fix}}$ yields BLS results that are consistent with the injected transit signal, while not removing the harmonic signal from light curves with $\Delta\chi^2_{\mathrm{Harm}} > \Delta\chi^2_{\mathrm{BLS,fix}}$ yields better results than removing the signal.

5. (Selection criteria sets 1 and 2 only) Finally, we attempt to remove any remaining instrumental or weather-related trends from the poststep-4 light curves using the Trend Filtering Algorithm (TFA; Kovács et al. 2005). This algorithm
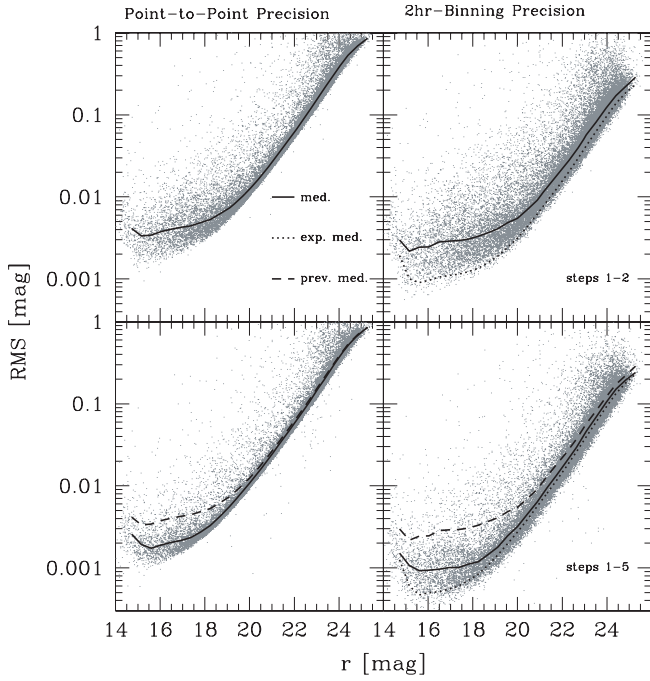
Figure 3. Light curve rms vs. r magnitude for $\sim$22,000 stars after completing steps 1–2 (top panels) and steps 1–5 (bottom panels) in the light-curve processing pipeline. We show both the point-to-point rms (left) and the rms after binning the light curves by 2 hr in time (right), which is approximately the timescale of a transit by an HJ. The solid lines show the median relation for the data plotted in each panel, while the dashed lines in the bottom two panels show the median relations from the top two panels. The dotted lines show the expected median relation for the binned light curves if the rms for each light curve were reduced by $N_b^{-0.5}$, where N_b is the average number of points in a time bin.

linearly decorrelates each light curve against a representative sample of other light curves. The trend list for each light curve consists of other stars on the chip with more than 2500 points, rms <0.1 mag, and that are well outside the photometric radius of the star in question. There are typically $\sim$250 stars in the trend list for each chip.

3.1.1. Light-Curve Precision

In Figure 3, we show the rms as a function of magnitude for the stars after stages 2 and 5 in the light-curve processing pipeline. We plot both the point-to-point rms and the rms after binning the light curves by 2 hr in time.

As discussed by Pont et al. (2006), the limiting factor for detecting low-amplitude transits around bright stars for many transit surveys is the presence of time-correlated systematic variations in the light curves (called red noise; noise that is uncorrelated in time will be referred to as white noise). We can estimate the degree of red noise in our light curves by fitting a noise model to the median rms–r relation. We use a model of the form:

$$\text{rms} = \sqrt{\left(\frac{2.5}{\ln(10.0)}\right)^2 \frac{f+s}{f^2} + \sigma_r^2}, \quad (2)$$

where $f = 10^{-0.4(m-z)}$ is the effective number of photoelectrons per image for a source of magnitude m with zero point z, $s = 10^{-0.4(m_s-z)}$ is the effective number of photoelectrons per image due to the sky that contaminate a given source and corresponds to a magnitude m_s, and σ_r is the effective red noise in magnitudes. Note that z depends on the aperture and efficiencies of the optics and detector, the exposure time, the

Table 1
Parameters from Fitting the Noise Model in Equation (2) to the Median rms–r Relations after Binning the Light Curves on Several Timescales

Binning Timescale (minutes)	z (mag)	σ_r (mmag)	m_{σ_r} (mag)[a]
5.0	32.45	1.35	17.57
10.0	32.81	1.21	17.68
30.0	33.46	1.04	17.90
60.0	33.95	1.00	18.21
120.0	34.44	0.92	18.43
180.0	34.64	0.90	18.53
240.0	34.63	0.93	18.58
1440.0	35.28	0.85	18.88
2880.0	37.38	0.47	19.37
7200.0	37.91	0.33	19.23
$m_s = 18.63$ mag			

Note. [a] The r-magnitude of a source that has equal red noise and white noise when the light curve is binned at the specified timescale.

atmospheric extinction, and the photometric procedure. Also note that m_s is the magnitude of a source, which has a flux equal to that of the total sky background through the effective photometric aperture. We bin the light curves on timescales of 5, 10, 30, 60, 120, 180, 240, 1440, 2880, and 7200 minutes and calculate the median rms–r relation for each binning. We then fit Equation (2) simultaneously to all 10 relations using the free parameters z_T, m_s and $\sigma_{r,T}$ where z_T and $\sigma_{r,T}$ depend on the timescale, while m_s is independent of the timescale. Table 1 gives the parameters from the model fit to the median rms–r relations. We also list in Table 1 the r-magnitude of a source for which the red noise on a given timescale is equal to the Poisson noise, that is,

$$\frac{2.5}{\ln(10)} \frac{\sqrt{f_T + s_T}}{f_T} = \sigma_{r,T}. \quad (3)$$

As expected, $\sigma_{r,T}$ decreases with increasing T. At the timescales relavent for a transit (1–3 hr), the red noise is $\sim$0.9 mmag. We also note that the values of z_T are consistent with the expected values given the gain of the detector and the measured zero point for the reference image, assuming that the effective exposure time for the "average" image in the light curve is $\sim$1.0 minute.

An alternative method to determine the degree of red noise in the data is to examine the autocorrelation function of the light curves. We find that stars fainter than $r\sim18.0$ are effectively uncorrelated in time while brighter stars appear to be uncorrelated on timescales longer than $\sim$200 minutes.

3.2. Transit Selection

To identify the best-fit transit signal in each light curve, we use the BLS algorithm. We apply two slight modifications to the algorithm.

1. Rather than searching over a fixed range of fractional transit width $q = \tau/P$ values (where τ is the duration of the transit and P is the orbital period), we allow the q range to vary with the trial frequency. We do this by assuming a stellar radius range of $R_{\min}$ to $R_{\max}$ and taking $q_{\min,\max} = 0.076 \left(R_{\min,\max} f\right)^{2/3}$, where f is the trial frequency in days^{-1}, and assuming that $M/M_\odot \approx R/R_\odot$ for lower main-sequence stars.

2. While the postprocessing described above substantially reduces the systematic variations in the light curves, some variations remain (see Figure 3). These variations give rise

to increased power at low frequencies in the BLS periodogram of each light curve. As a result, long-period transits should be treated with greater caution than short-period transits. To account for this, we subtract a mean-filtered periodogram from the raw periodogram for each light curve before selecting the peak frequency. To mean filter the periodogram we replace each point in the periodogram by the mean value of the 200 points closest in frequency to the given point after applying an iterative 3σ clipping. Testing this modification on light curves with injected transits shows a very slight improvement (less than 1%) in the fraction of light curves for which the recovered period agrees with the injected period.

We conduct both a high-resolution and a low-resolution BLS search on the light curves. The low-resolution search is needed for the transit recovery simulations (Section 5.1.1) to finish in a reasonable amount of time. For the high-resolution search we examine 20,000 frequency values over a period range from 0.2 to 5.0 days using 200 phase bins at each trial frequency, using $R_{min} = 0.4\,R_\odot$ and $R_{max} = 1.3\,R_\odot$. For the low resolution search we examine 3072 frequency values over the same period range, using the same number of phase bins. In searching for candidates with the low-resolution search, we use parameters identical to those used in conducting the transit recovery simulations (Section 5.1.1). We use slightly different parameters for possible cluster members and for field stars (see the selections of these stars in Sections 5.1.2 and 5.2). For candidate cluster members, we take $R_{min} = 0.1\,R_\odot$ and $R_{max} = 1.1 \times R_{phot}$, where R_{phot} is the radius of the star estimated from its photometry assuming that it is a cluster member. For the field stars, we take $R_{min} = 0.1\,R_\odot$ and $R_{max} = 1.3\,R_\odot$.

As discussed by B06, a simple selection on the Signal Residue (Equation (5) in Kovács et al. 2002) or the Signal Detection Efficiency (Equation (6) in Kovács et al. 2002) generally yields a large number of false positive detections that must then be removed by eye. However, because it is very difficult to accurately include by eye selections in a Monte Carlo simulation of the transit selection process, it is necessary to devise automatic selection criteria that minimize the number of false positive detections to calculate a robust limit on the frequency of stars with planets. We discuss the three distinct selection criteria that we have devised in turn.

3.2.1. Selection Criteria Set 1

To devise the first set of selection criteria we inject fake transit signals into the light curves of 1366 stars that lie near the cluster main sequence on a color–magnitude diagram (CMD) and choose criteria that maximize the selection of high signal-to-noise-simulated transits, while minimizing the selection of false positives. The simulated transits have radii of 0.35, 0.71 and 1.0 R_J, and inclinations of 90°. For each star/radius, we simulate 10 transits with periods ranging from 0.5 to 5.0 days and random phases. We use the relations between r-magnitude and mass, and r-magnitude and radius for the cluster that were determined in Paper I to estimate the mass and radius of each star. The light curves including injected transits are passed through the pipeline described in the previous subsection before running the BLS algorithm on them.

To calibrate the selection criteria, we first must define the set of injected transits that we consider to be recoverable; we then adopt selection criteria that maximize the selection of these light curves while minimizing the selection of all other light curves. Note that we use information from the injected transits

to define the recoverable sample, while we cannot use any of this information when defining the selection criteria. We consider the transit to be recoverable if $\Delta\chi^2_{BLS} - \Delta\chi^2_{BLS,0} < -100$, where $\Delta\chi^2_{BLS}$ is the reduction in χ^2 for the best-fit BLS model to the light curve with the injected transit and $\Delta\chi^2_{BLS,0}$ is for the light curve prior to injecting the transit. When a light curve satisfies this criterion, the best-fit BLS model is strongly influenced by the transit signal. This can happen even if the identified period does not match the injected period, or a harmonic of the injected period, however, in these cases, detailed follow up may eventually yield the correct period. Note that for transit selection criteria sets 2 and 3, we adopt the more conservative recoverability criterion that the recovered period must match the injected period, or one of its harmonics, to within 10%.

We find that the following selection criteria accurately distinguish between the recoverable and nonrecoverable transits.

1. Following B06, we use BLS to identify both the best-fit transit signal and the best-fit inverse transit signal for each light curve. For the best-fit transit signal, we calculate the signal-to-pink-noise (SN) ratio (Pont et al. 2006) via

$$SN^2 = \frac{\delta^2}{\sigma_w^2/n_t + \sigma_r^2/N_t},\qquad(4)$$

   where δ is the depth of the transit, n_t is the number of points in the transit, N_t is the number of distinct transits sampled, σ_w is the white noise, and σ_r is the red noise at the timescale of the transit. To calculate the white noise for a light curve, we subtract the best-fit BLS model from the light curve and set σ_w equal to the standard deviation of the residual. To calculate the red noise, we bin the residual light curve in time with a bin size equal to the duration of the transit and set σ_r equal to its standard deviation. Note that while this technique provides a convenient method to determine an individual red and white noise estimate for each light curve, it overestimates the noise for an uncorrelated signal by a factor of $\sim\sqrt{2}$. We select candidates that have $SN > 10.0$. Figure 4 shows this selection.

2. As shown in Figure 4, some of the transit signals that are not expected to be detectable pass the selection from the previous step. We can further reduce these potential false alarms with negligible loss of detectable transits by the following selection. Let $\Delta\chi^2_{BLS}$ refer to the reduction in χ^2 for the best-fit transit signal and $\Delta\chi^2_{BLS,2}$ refer to the reduction in χ^2 for the second noninverse transit peak in the BLS spectrum. The light curves passing selection 1 are then selected if they have $P > 2.0$ days and $\Delta\chi^2_{BLS} - \Delta\chi^2_{BLS,2} < -60$ or $P \leqslant 2.0$ days and $\Delta\chi^2_{BLS} - \Delta\chi^2_{BLS,2} > -10.95P^{2.45}$, as shown in Figure 5.

When the above selections are applied to the actual data, more than 100 light curves are selected. Many of these are obvious false positives that can be eliminated by applying a few additional selections.

3. We reject stars with fewer than 1000 points in their light curves; most of these are near saturation and show strong systematic variations even after applying the TFA.

4. Many of the false positives are faint stars located near much brighter stars; these can be rejected by only considering stars with an average instrumental magnitude brighter than 17.0 (corresponding roughly to $r < 22.0$).
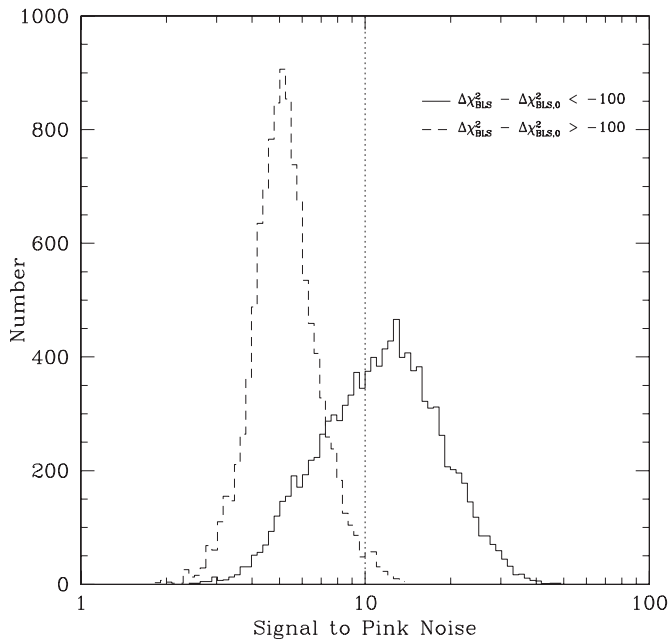
Figure 4. Histograms of the SN of light curves with injected transit signals. We show separate histograms for injected transits that should be recoverable ($\Delta\chi^2_{BLS} - \Delta\chi^2_{BLS,0} < -100$) and for those that may be unrecoverable. Light curves with $SN > 10.0$ are selected.
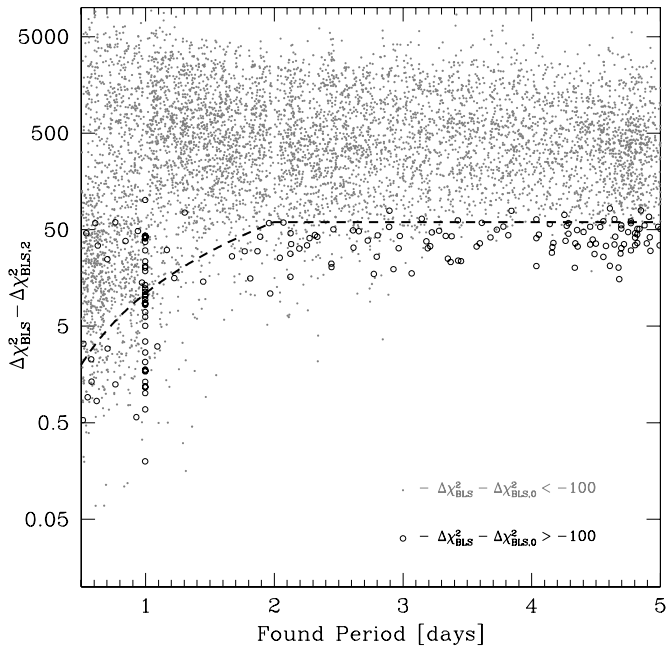

Figure 5. Difference in χ^2 reduction from the best-fit box-car transit model and the second best-fit model vs. the period of the best-fit model for light curves that pass the selection in Figure 4. Light curves below the dashed line are rejected.

5. Other false positives come from very noisy light curves that can be rejected by requiring the standard deviation of the residual light curve after subtracting the best-fit box-car transit model to be less than 0.1 mag.

6. Many false positives show an anomalous faint set of points that occur on only one night. Following B06, we require that the fraction of $\Delta\chi^2_{BLS}$ that comes from one night must be less than 0.8.

7. We reject light curves for which the best-fit box-car transit has a period between 0.99 and 1.02 days or less than 0.4 days.
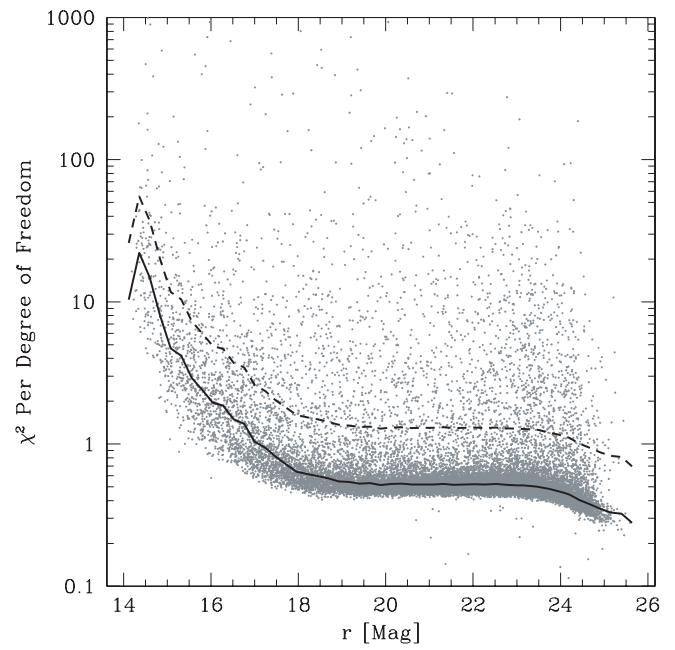

Figure 6. χ^2 per dof of the light curves without injected transits after subtracting the best-fit box-car transit model. The solid line shows the median χ^2 per dof as a function of magnitude. Light curves above the dashed line (2.5 times the solid line) are rejected as transit candidates. See the text for a discussion of why χ^2 per dof for stars between $18 \lesssim r \lesssim 23$ approaches ~ 0.5 rather than ~ 1.0.

8. Finally, we require that χ^2 per degree of freedom (dof) of the light-curve residual after subtracting the best-fit box-car transit model must be less than 2.5 times the expected χ^2 per dof. The expected χ^2 per dof is taken to be the median value as a function of magnitude for the full ensemble of light curves (Figure 6). Note that the values of χ^2 per dof for stars between $18 \lesssim r \lesssim 23$ approach ~ 0.5 rather than ~ 1.0. This is due to a bug in our differential photometry routine whereby the formal differential flux uncertainties returned are not set to the flux scale of the reference image. We note that a similar bug is present in the differential photometry routine of the ISIS 2.1 package on which our photometry routine is based. The flux scale for the reference image that we use is set to that of a 30 s exposure taken under good seeing conditions. The formal errors are overestimated for longer exposures that were taken under poor seeing conditions. We identified this bug after completing most of the analysis presented in this paper; we do not, however, expect it to significantly affect the statistical results presented here. Note that since the photometry that we are using is dominated by red noise, rather than white noise, the formal photometric errors, which assume Gaussian, uncorrelated noise, do not accurately describe the uncertainties in the data. We have therefore used a cut on the SN, which is determined empirically from the light curve, rather than relying on the formal uncertainties. The formal uncertainties do affect the relative weightings of points; modifying them may thus yield slight changes in the TFA fitting procedure as well as in the periods that are identified by BLS. If the formally correct weighting scheme had been adopted, the sample of selected candidates may have been slightly different; however, this is no different from making minor changes to the rather arbitrary selection criteria. For our statistical conclusions regarding the fraction of stars bearing planets,

what is important is that we apply the same selections and weighting scheme to the transit injection simulations as we do to the actual data and that the postselection vetting procedure that we apply to the actual data would not reject any of the injected candidates. Making a uniform change to the weighting scheme will affect the selection of real candidates and injected transits in the same manner, so the transit detection efficiency measured by the injection simulations will accurately reflect the detection efficiency for the survey.

3.2.2. Selection Criteria Set 2

The above selection criteria were developed by manually inspecting the results of transit recovery simulations and defining cuts that appeared, by eye, to distinguish between successful recoveries and nonrecoveries. While this method has the advantage that the criteria can be enumerated and easily visualized, it has the disadvantage that the cuts are fairly subjective and there is no guarantee that the selections optimally distinguish between recoveries and nonrecoveries.

To complement the above selection criteria, we have devised a set of selections using the Support Vector Machine (SVM) classification algorithm, which has the advantage of being much less subjective, but the disadvantage of being difficult to visualize (Vapnik 1995; a discussion of the algorithm can also be found in Press et al. 2007, which we summarize here). This algorithm takes as input a set of training data, which consists of m points, $(\mathbf{x}_i, y_i)$, where $\mathbf{x}_i$ is an n-dimensional vector of measurable parameters describing object i (called features) and y_i is either $+1$ or -1 and is used to divide the data into two classes. The algorithm then searches for a real-valued function $f(\mathbf{x})$ such that $f(\mathbf{x}_i) > 0$ for $y_i > 0$ and $f(\mathbf{x}_i) < 0$ for $y_i < 0$. The function is assumed to take the form

$$f(\mathbf{x}) = \mathbf{W} \cdot \phi(\mathbf{x}) + B, \qquad (5)$$

where $\phi(\mathbf{x})$ is a fixed n-to-N-dimensional transformation with N being typically larger than n, and $\mathbf{W}$ is an N-dimensional vector. To optimize f, one looks for a vector $\mathbf{W}$ that is normal to a hyperplane that separates $\phi(\mathbf{x}_i)$ with $y_i = +1$ from $\phi(\mathbf{x}_i)$ with $y_i = -1$ and that has a maximum perpendicular distance from the points nearest to it (called support vectors). In general, it is not always possible to find such a hyperplane, so instead one seeks to optimize f by minimizing

$$\frac{1}{2}\mathbf{W} \cdot \mathbf{W} + \lambda \sum_i \Xi_i \qquad (6)$$

subject to the constraint

$$\Xi_i \geqslant 0, \quad y_i f(\mathbf{x}_i) \geqslant 1 - \Xi_i, \quad i = 1, \ldots, m, \qquad (7)$$

where Ξ_i are free parameters that allow for discrepancies between the model and actual classes and λ is a fixed regularization parameter used to control the tradeoff between accurately classifying the training data and maximizing the perpendicular distance between the support vectors and the hyperplane. In practice, the problem is recast in the Lagrangian formalism so that one specifies a kernel matrix with the property $K_{ij} = K(\mathbf{x}_i, \mathbf{x}_j) = \phi(\mathbf{x_i}) \cdot \phi(\mathbf{x_j})$ rather than the transformation $\phi(\mathbf{x})$.

To apply the SVM algorithm to our problem of devising transit selection criteria we use the *SVMlight* package[8] (Joachims 1999,

---

[8] C source code for *SVMlight* is freely available at http://svmlight.joachims.org.

2002). Before using the algorithm, we apply a set of simple cuts which we found to be necessary to minimize the number of false positives.

1. Reject stars with an average instrumental magnitude fainter than 17.0 (corresponding roughly to $r > 22.0$).
2. Reject stars that have rms > 0.1 mag, where the rms here is the standard deviation of the residual light curve after subtracting the best-fit box-car transit model.
3. Reject stars with $SN < 10.0$, where SN is the SN given by Equation (4). Note for training the algorithm, we use a less restrictive cut of $SN < 9.0$.
4. Reject light curves for which the best-fit box-car transit has a period between 0.99 and 1.02 days or less than 0.4 days.

We train the algorithm on the simulated transit data described in Section 5.1.1. We use only ~ 5000 of the ~ 250 million simulated transits to allow the algorithm to converge in a reasonable amount of time. We take $y_i = +1$ for simulated transits that have $0.95 < P_{\text{recover}}/P_{\text{inject}} < 1.05$, where P_{recover} and P_{inject} are the recovered and injected transit periods, respectively, and $y_i = -1$ for all other simulated transits. There are 15 features in the $\mathbf{x}_i$ vectors including: the recovered period, the fractional transit width, the transit depth, SN, the white noise, the red noise, $\Delta\chi^2_{\text{BLS}}$, $\Delta\chi^2_{\text{BLS}}/\Delta\chi^2_{\text{BLS,inv}}$, $(\Delta\chi^2_{\text{BLS,2}} - \Delta\chi^2_{\text{BLS}})/\Delta\chi^2_{\text{BLS}}$, the fraction of $\Delta\chi^2_{\text{BLS}}$ that comes from one night, the number of points in transit, the number of points observed less than τ minutes prior to transit ingress (τ is the duration of the transit), the number of points observed less than τ minutes after transit egress, the number of distinct transits observed, and the ratio of χ^2 per dof of the light-curve residual after subtracting the best-fit box-car transit model to the expected χ^2 per dof. When applying the algorithm, we consider a transit to be recovered if the estimated value of y is greater than 0.1 as we found a number of false positives for which the algorithm returned values between 0.0 and 0.1.

3.2.3. Selection Criteria Set 3

As described in Section 6, when the first two sets of selection criteria are applied to transit recovery simulations the detection efficiency for $1.5R_J$ and larger planets drops unexpectedly for relatively bright stars. These large radius planets yield deep transit signals in the light curves of bright stars, which are then distorted by steps 3–5 of the processing routines described in Section 3.1. To recover these large radii planets, we have devised a third set of selection criteria. For this set of criteria, we run BLS on light curves processed through steps 1 and 2 of Section 3.1 (i.e., we do not remove one sidereal day period signals from the light curves, remove harmonic signals from the light curves, or apply the TFA to the light curves). We then apply the SVM classification algorithm to the BLS results using the same training scheme and set of features as in Section 3.2.2. We train only on 1.0, 1.5, and $2.0R_J$ simulations.

4. TRANSIT CANDIDATES

Out of a total of 10,899 light curves for sources that were detected in g, r, and i have an average instrumental magnitude brighter than 17 ($r \lesssim 22$), and more than 1000 points, we select 16 transit candidates. Table 2 lists the candidates, their coordinates, photometry and BLS parameters and the selection criteria/resolutions that selected them. Phased light curves for the candidates are displayed in Figure 7. As we discuss below, 12 of these candidates can be rejected as eclipsing binary stars

Table 2
Candidate Transiting Planets

ID	R.A. (J2000)	decl. (J2000)	g^a	r^a	i^a	B^b	V^b	I^c	Selection[d]	LC[e]	Period (days)	MJD_0	Depth (mag)	q	S/N[f]
30137	05:52:53.99	+32:39:11.7	20.86	19.74	18.95	21.20	19.94	18.50	011000111	2	0.595950	53725.32142	0.0423	0.085	24.24
60161	05:53:18.26	+32:29:46.7	20.42	19.57	19.11	20.97	19.91	18.67	001000000	2	2.623233	53726.80688	0.0484	0.045	11.79
70127	05:53:18.46	+32:28:33.3	20.47	19.58	19.02	21.00	19.85	18.57	010000110	1	0.773530	53725.31696	0.0197	0.060	10.57
80009	05:53:02.04	+32:23:27.6	15.75	15.09	14.76	16.13	15.30	14.32	000000001	3	1.519846	53724.56637	0.0483	0.045	12.29
80014	05:53:12.12	+32:23:51.2	16.28	15.77	15.46	16.62	15.92	15.03	001001000	2	0.588375	53725.61226	0.0054	0.100	13.22
90279	05:52:53.06	+32:22:57.0	23.58	21.87	20.45	24.37	22.43	19.96	111000111	2	1.141717	53726.05590	0.3173	0.045	37.23
110021	05:52:26.24	+32:40:44.6	16.36	15.77	15.43	16.77	15.99	14.99	000010000	3	3.535574	53727.68767	0.1215	0.035	13.35
120050	05:52:46.14	+32:39:33.6	17.71	16.98	16.55	18.20	17.35	16.11	111111000	3	1.847414	53725.76532	0.0346	0.045	14.90
160017	05:52:23.89	+32:28:26.3	16.31	15.60	15.24	16.75	15.90	14.81	000110000	3	1.560626	53724.96524	0.0141	0.055	4.37
160311	05:52:19.64	+32:26:50.4	23.20	21.63	20.64	23.78	22.26	20.17	111000111	2	2.027186	53726.18244	0.1789	0.025	26.33
170049	05:52:44.65	+32:25:55.3	18.36	17.65	17.30	18.74	17.90	16.87	000000001	2	2.261081	53725.22479	0.0181	0.055	10.29
170100	05:52:38.44	+32:23:29.5	20.34	18.73	17.80	21.02	19.43	17.34	000001000	3	2.746378	53725.19817	0.2963	0.025	20.78
230082	05:52:01.32	+32:32:51.0	17.71	17.08	16.71	18.15	17.36	16.27	011000011	2	3.335057	53726.43670	0.0280	0.025	15.05
270149	05:51:59.04	+32:20:38.0	20.59	19.47	18.87	21.68	19.98	18.42	000000111	3	1.097491	53724.89160	0.2132	0.065	11.11
280287	05:51:37.41	+32:45:03.0	23.80	22.12	20.78	24.68	22.82	20.29	111000011	2	0.456034	53725.41220	0.1331	0.055	17.35
330224	05:51:30.37	+32:30:29.3	21.64	20.46	19.91	22.11	20.94	19.46	010000110	1	0.648749	53725.20636	0.0502	0.060	13.79

Notes.
[a] The magnitude of the source in the photometric catalog (Paper I).
[b] Value from Kalirai et al. (2001).
[c] Value from transforming ri photometry to the I_C photometry of Nilakshi & Sagar (2002).
[d] 9 bit flag to indicate which selection criteria sets and resolutions selected the candidate. From the left, the first 3 bits indicate if the candidate was selected by criteria sets 1, 2, and 3, respectively, using a high-resolution BLS search. The middle 3 bits are for the low-resolution BLS search applied to candidate cluster members, while the last 3 bits are for the low-resolution BLS search applied to field stars.
[e] This integer indicates if the BLS parameters in this table were determined for (1) the fully processed, trend-filtered light curve, (2) the light curve processed through steps 1 and 2 of Section 3.1 only, or (3) the unprocessed light curve.
[f] SN ratio (Equation (4)).

by their large transit depths or by noting that the primary and secondary transit depths are unequal. Two of the candidates detected on the unprocessed light curves result from artifacts in the data, which are removed by the processing routines. One of the candidates is a blend with a nearby deep eclipsing binary. One candidate Jupiter-sized transiting planet remains.

As seen in Figure 8, several of the candidates (80014, 110021, 120050, 160017, and 170100) lie close enough to the cluster main sequence on the $g-r$ and $g-i$ CMDs to be selected as potential cluster members in Section 5.1; however, all of these candidates can be rejected as either eclipsing binaries or a blend with an eclipsing binary (see Section 4.1). We can therefore only place an upper limit on the planet occurrence frequency of cluster members.

4.1. Discussion of Individual Transit Candidates

30137. This source is an eclipsing binary as evidenced by the secondary eclipse having an unequal depth to the primary eclipse when phased at twice the period shown in Figure 7. This source is V1187 in the catalog of variables presented in Paper II. We reject this candidate.

60161. The transitlike variation in this light curve is completely removed by the TFA so this source only passes selection criteria set 3. The transit feature is due primarily to two nights. The images on these nights show a gradient in the background counts near the corner of Chip 6 where this star is located. The sense of the gradient is that points are fainter in the corner than near the center of the image. The use of a single master flat-field image for the entire run appears to have failed for these two nights; the result is that many of the stars in the corner of Chip 6 show dips in their raw light curves on the two nights in question. This transit feature therefore appears to be spurious,

and we reject it as such. We note that this is the only candidate that was selected by the high-resolution search but not by the low-resolution search.

70127. This source is a promising transit candidate around a field star. Crosscorrelation analysis of the Hectochelle spectrum for the source yields $T_{eff} \sim 5000$ K though the uncertainty is very high due to the faintness of the source. Note that there is a nearby source to 70127 that may also contaminate this spectrum. Combining the B, V, and I_C photometry for the source, we estimate that $(B-V)_0 \sim 1.0$, and $E(B-V) \sim 0.16$ so that the star has a radius of $R_\star \sim 0.75 R_\odot$ and a mass of $M_\star \sim 0.8\ M_\odot$. The light curve has Tingley & Sackett (2005) parameters of $\eta_p = 0.7$ and $\eta_\star = 0.7$, so it appears to be consistent with the transiting planet hypothesis. The source is located less than $2''$ from the edge of the chip; this appears to add some scatter to the light curve that is correlated with the seeing and removed by the TFA. Also note that there is a 1.625 mag fainter source, 70181, that is located only $0.''8$ from 70127. The fainter source also shows a dip in its light curve; however, the dip in flux appears to be greater for 70127 than 70181, and the centroid of 70181 on the residual image appears to shift slightly in phase with the transit, whereas 70127 does not. Both of these factors suggest that 70127 is the real variable. The "shoulder" just before transit is an artifact of postprocessing the fairly high signal-to-noise light curve and does not appear in the unprocessed light curve. Fitting a Mandel & Agol (2002) transit model to the light curve with quadratic limb darkening coefficients fixed to $u_1 = 0.54$ and $u_2 = 0.2$ from Claret (2004), which are appropriate for a ~ 5000 K dwarf star in the r filter, and fixing $a/R_\star = 4.38$ assuming the stellar mass, radius, and the orbital period of 0.77353 days, we find $R_P \sim 1.0 R_J$ and $\sin i \sim 0.99$. The expected RV amplitude for the star would be $K \sim 220$ m s^{-1} (M_P/M_J), where M_P is the mass of the planet. To rule out astrophysical false positives, such
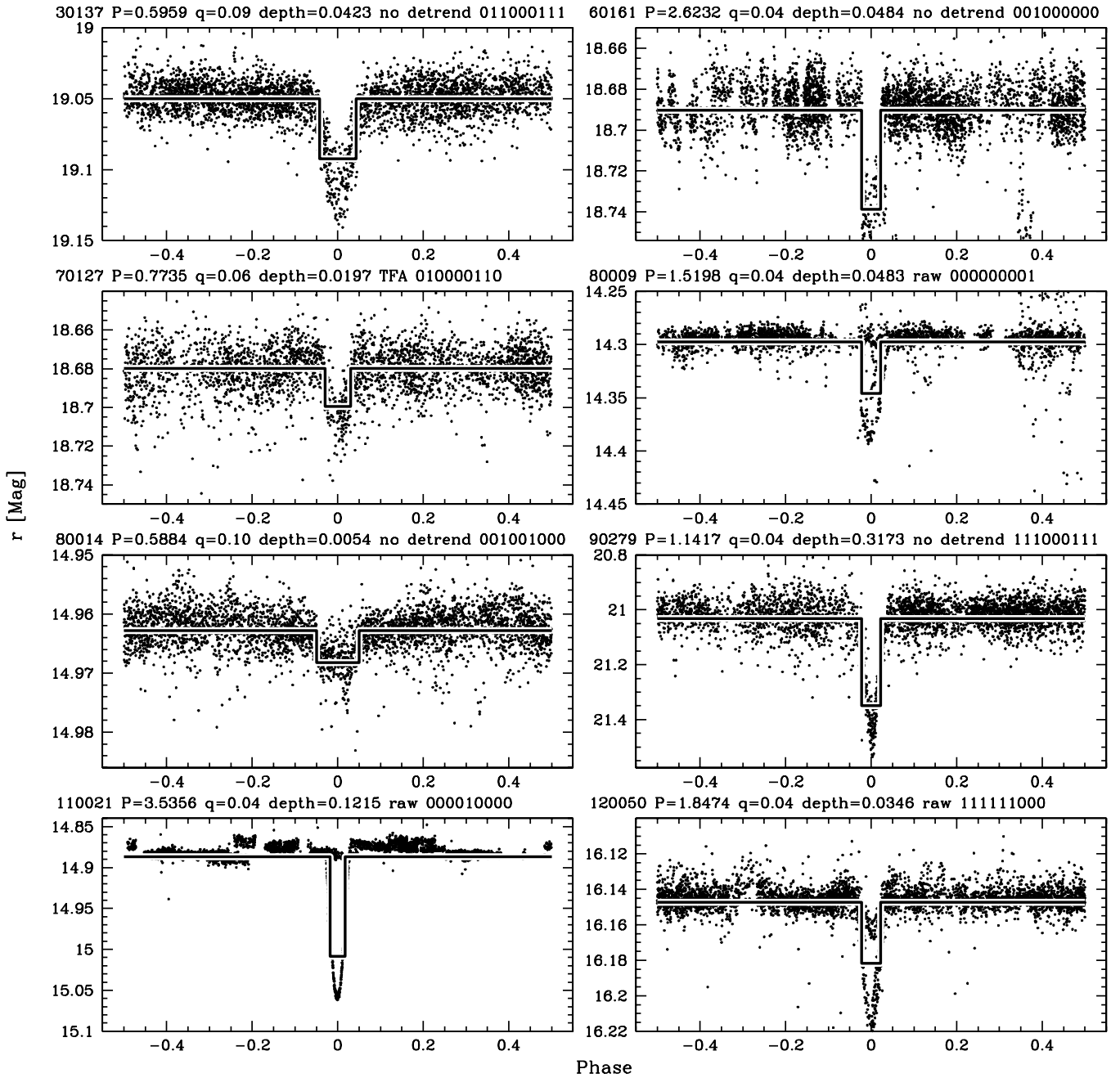
Figure 7. Phased light curves for 16 candidate transiting planets selected by the pipeline discussed in Section 3.2. See Section 4.1 for a discussion of each candidate. The ID is taken from the photometric catalog presented in Paper I. We list for each candidate the period in days, the fractional transit width q, and the transit depth in magnitudes returned by BLS. We note whether the displayed light curve has been processed through the full pipeline (TFA), through steps 1 and 2 only of Section 3.1 (no detrend), or if no processing has been applied (raw). We show raw light curves for a handful of candidates where σ-clipping removes some of the in-transit points. We also display a 9 bit flag to indicate which selection criteria sets and resolutions selected the candidate. From the left, the first 3 bits indicate if the candidate was selected by selection criteria sets 1, 2, and 3, respectively, using a high-resolution BLS search. The middle 3 bits are for the low-resolution BLS search applied to candidate cluster members, while the last 3 bits are for the low-resolution BLS search applied to field stars.

as an M-dwarf secondary, would require additional follow-up spectroscopy which would be challenging given the faintness of the source ($r\sim$19.6, $V = 19.85$). Note that Sahu et al. (2006) achieved a formal RV precision of $\sim$200 m s^{-1} for their candidate SWEEPS-11, which has a comparable magnitude ($V = 19.83$), so conducting spectroscopic follow up for 70127 is not beyond the realm of possibility.

80009. This source appears to be an eclipsing binary, though there is not enough data to determine the period. There is a

significant amount of scatter in the light curve that results from the source being nearly saturated. From the B, V, and I_C photometry, we estimate that the reddening to the source is $E(B-V)\sim 0.18$ so that the source would have $(B-V)_0 \sim 0.65$ and $M \sim 1.0$ $M_\odot$. The primary eclipse depth appears to be deeper than the value returned by BLS (closer to $\sim$0.1 mag); the secondary source would have to be significantly larger than $2.0 R_J$ to create such a deep eclipse for this star. We reject this candidate.
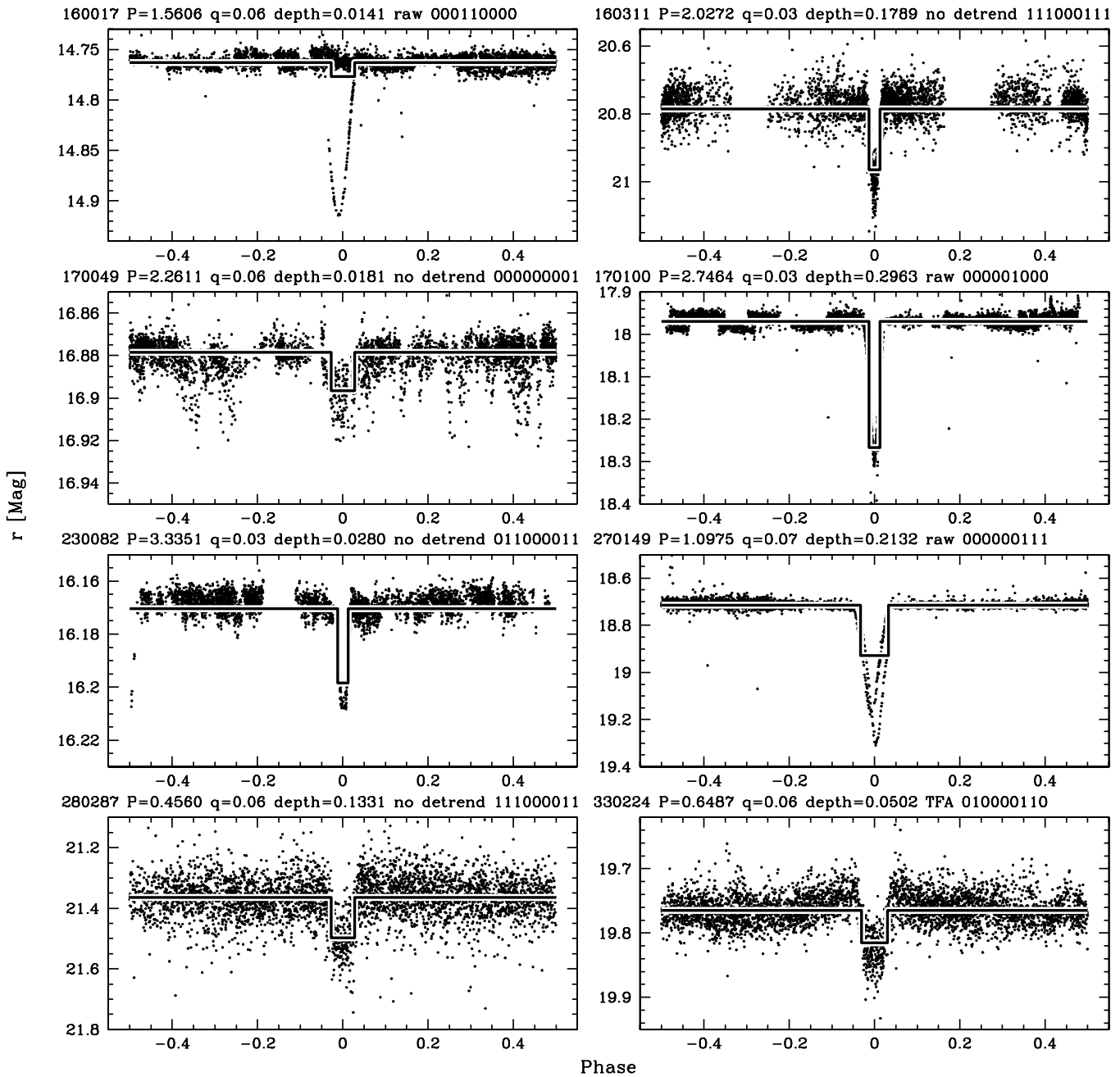
Figure 7. (Continued)

80014. This shallow transit-like signal is the result of a blend with the $r \sim 18.3$ mag eclipsing binary, V29, that is located $\sim 3''$ away. We reject this candidate.

90279. This is an eclipsing binary with a period of 2.283 days. Phasing the light curve at twice the period shown in Figure 7 reveals that the secondary and primary eclipses are slightly unequal in depth. It is V1182 in the catalog of variables presented in Paper II. We reject this candidate.

110021. This source is a candidate cluster member with an estimated mass of $\sim 1.2\ M_\odot$. The secondary object must be significantly larger than $2.0 R_J$ to yield an eclipse deeper than 0.1 mag; the source is thus an eclipsing binary. The source is V827 in the catalog of variables presented in Paper II. The period displayed in Figure 7 and listed in Table 2 is the period returned by BLS. When phased at a period of 6.7667 days the

presence of a secondary eclipse becomes apparent; it is also apparent that the system has significant eccentricity as well as an out-of-eclipse variation that phases with the proper orbital period. We reject this candidate.

120050. This is an eclipsing binary; note the dual eclipse depths at phase 0.0. When phased at twice the period shown in Figure 7, it is clear that the light curve shows primary and secondary eclipses of differing depths. This source is V140 in the catalog of variables presented in Paper II. We reject this candidate.

160017. This source is an eclipsing binary. Its position on the CMD makes it a candidate cluster member with a mass of $\sim 1.2\ M_\odot$. For such a primary, the deep eclipse could not be caused by a planetary-sized companion. There is an out-of-eclipse variation that phases at 4.0989 days; however, the
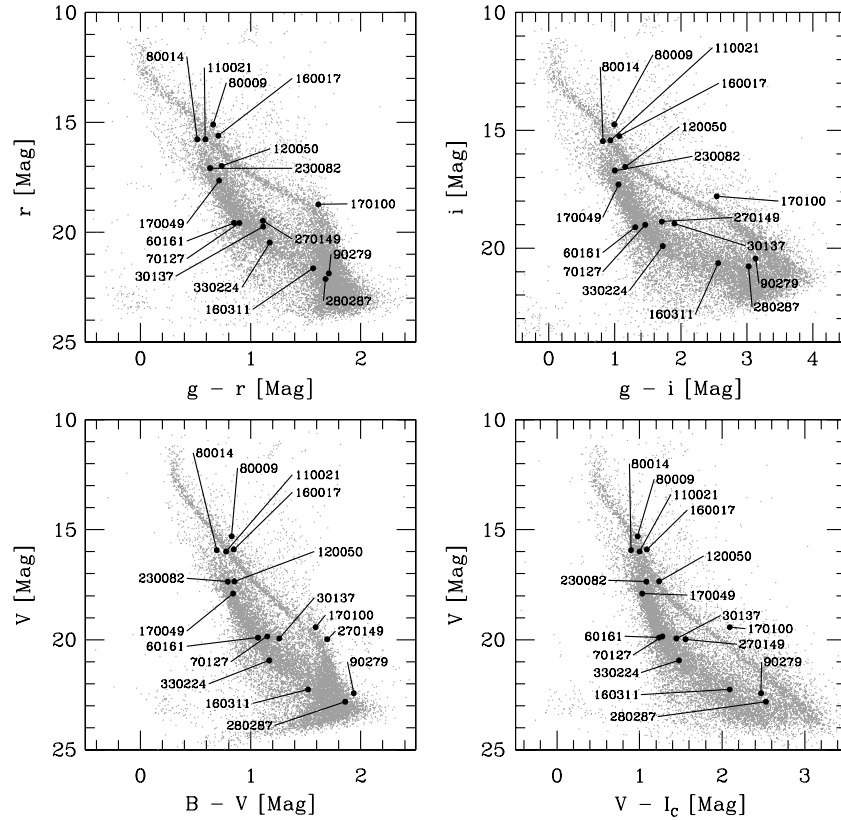
Figure 8. Location of 16 candidate transiting planets on $g-r$, $g-i$, $B-V$, and $V-I_C$ CMDs. The light points show all stars; the dark points show the transit candidates. Five of the candidates lie near enough to the cluster main sequence on the $g-r$ and $g-i$ CMDs to be selected as potential cluster members (see Figure 9).

eclipses do not phase at this period. There is not enough data to accurately determine the orbital period. In Figure 7, we show the raw light curve phased at the period returned by BLS for the light curve processed through the TFA. The parameters listed in Table 2 for this system are for the raw light curve, the S/N value is well below 10.0 in this case. The σ-clipping routine clips much of the eclipse yielding a shallow transit that phases roughly at the period shown and yields an S/N value above 10.0. This source is V791 in the catalog of variables presented in Paper II. We reject this candidate.

160311. This is an eclipsing binary; there is a shallow secondary eclipse with a depth of ∼0.05 mag visible at phase 0.5. This source is V716 in the catalog of variables presented in Paper II. We reject this candidate.

170049. The transit feature seen in the noisy unprocessed light curve is completely eliminated by TFA. The source lies within 2″ of the edge of the frame and the variations in the light curve are strongly correlated with the image seeing. The transit feature is removed when the light curve is decorrelated against seeing. We reject this candidate as the variations appear to be spurious.

170100. This source is an eclipsing binary. When phased at twice the period displayed in Figure 7, it is clear that the primary and secondary eclipses are of unequal depth. The out-of-eclipse variations also phase at this period. This source is V1028 in the catalog of variables presented in Paper II. We reject this candidate.

230082. This source, V485, is most likely an F–M eclipsing binary. Note that when phased at the period recovered by BLS (as shown in Figure 7), there appears to be a secondary eclipse at

phase −0.5, when phased at a period of 1.6676 days; however, the putative secondary matches to the primary eclipse. Also note that the clipping procedure removes some points from the bottom of the eclipse; the eclipse in the raw light curve is ∼0.01 mag deeper. From the B, V, and I_C photometry, we estimate $E(B − V) ∼ 0.38$, so $(B − V)_0 ∼ 0.41$, which corresponds to a ∼1.5 $M_\odot$, and ∼1.4$R_\odot$, primary star. For a star of this size, a 0.034 mag transit requires that the companion have a radius greater than $2R_J$.

270149. This source, V457, is an eclipsing binary. Note the deep, and distinct, primary and secondary eclipses. We plot the raw light curve for this star in Figure 7; the clipping routine removed many of the points in eclipse, which caused BLS to identify the wrong period and underestimate the depth.

280287. This is a grazing eclipsing binary. When the raw light curve is phased at twice the period found by BLS, it is clear that the primary and secondary minima are of unequal depths. This source is V226 in the catalog of variables presented in Paper II. We reject this candidate.

330224. This source, V141 in the catalog of variables, is an eclipsing binary given its depth. The raw light curve reveals a strong out-of-eclipse variation with a peak-to-peak amplitude of ∼0.1 mag that phases at the orbital period.

5. TRANSIT DETECTION EFFICIENCY CALCULATION

To calculate our planet detection efficiency, we follow the procedure described by B06; we summarize the procedure here and perform the calculation separately for cluster members and field stars.
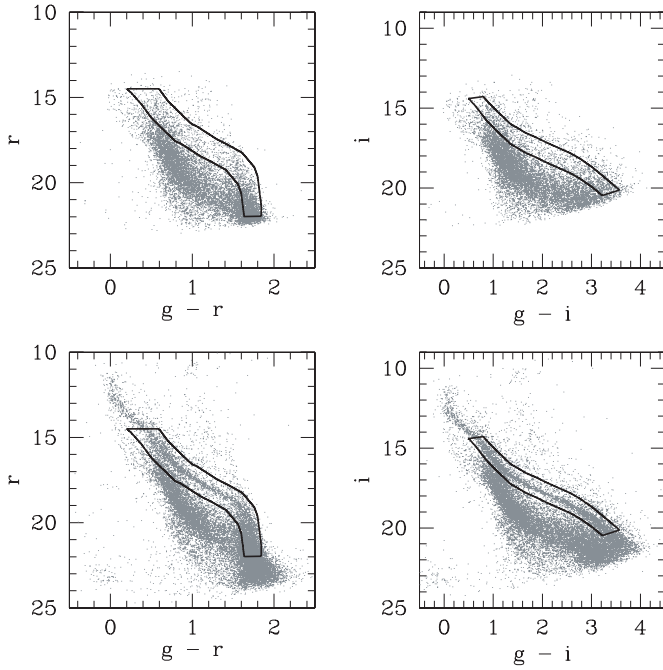
Figure 9. Selection of stars near the cluster main sequence, which are used in computing the planet detection probability, is plotted on $g-r$ and $g-i$ CMDs. The bottom two panels show the CMDs for the field on the cluster, while the top two panels show the CMDs for a field adjacent to the cluster with the same Galactic latitude (see Paper I). The off-cluster field is used in determining the membership probability as a function of magnitude (Figure 10). Stars falling within the solid black lines on both CMDs are selected as stars near the cluster main sequence.

5.1. Cluster Members

In Figure 9, we show the selection of stars near the cluster main sequence on $g-r$ and $g-i$ CMDs. We select a total of 2475 stars that have an instrumental magnitude of less than 17, rms <0.1 mag, and that have at least 1000 points in their light curves. Note that we expect ~1450 of these stars to be cluster members. We use these stars to place a limit on the planet occurrence frequency for the cluster. The total number of planets in the cluster that we expect to detect with our survey is given by

$$N_{\rm det} = f \sum_{i=1}^{N} P_{{\rm det},i}, \qquad (8)$$

where f is the planet occurrence frequency over a specified planet radius and orbital period range, $P_{{\rm det},i}$ is the probability of having detected such a planet for star i, and there are N candidate cluster members in the survey. For a binomial distribution, the detection of no planets is inconsistent at the ~95% level when $N_{\rm det} \gtrsim 3$. The 95% confidence upper limit on the planet occurrence frequency is then

$$f \leqslant 3 \Big/ \left(\sum_{i=1}^{N} P_{{\rm det},i} \right). \qquad (9)$$

The planet detection probability for star i is given by

$$P_{{\rm det},i} = \iint \frac{d^2 p}{dR_p dP} P_{\epsilon,i}(P, R_p) P_{T,i}(P, R_p) P_{{\rm mem},i} dR_p dP, \qquad (10)$$

where $P_{\epsilon,i}$ is the probability of detecting a transit of a planet with the orbital period P and radius R_p for star i if it has an

orbital inclination that yields transits, $P_{T,i}$ is the probability that the planet has an inclination that yields transits, $P_{{\rm mem},i}$ is the probability that star i is a cluster member, and $d^2 p/dR_p dP$ is the joint probability distribution of R_p and P.

There are four terms that contribute to Equation (10) that must be determined separately. Assuming random orientations, the term $P_{T,i}$ is given analytically by $P_T = (R_\star + R_p)/a$, where $R_\star$ is the radius of the star and a is the semimajor axis for an orbital period P and stellar mass $M_\star$. For the term $P_{{\rm mem},i}$ we take the photometric membership probability of the star, which we calculate by comparing the CMD of the cluster to a CMD of a field off the cluster. The term $d^2 p/dR_p dP$ must be treated as a prior, and the term $P_{\epsilon,i}$ is calculated via Monte Carlo simulation as discussed below.

5.1.1. Calculating $P_{\epsilon,i}$

We follow the procedure described by B06 to calculate $P_{\epsilon,i}$. This involves injecting limb-darkened transits into the light curves of potential cluster members and attempting to recover them. Transits are injected into the raw light curves; we then run each simulated light curve through the postprocessing and transit selection routines described in Section 3. Note that we only conduct simulations on light curves that are not selected as transit candidates. Since there are only a few candidates, not including their efficiencies should not change our results significantly.

To simulate transit light curves, we use the Mandel & Agol (2002) analytic model with r-band quadratic limb-darkening coefficients from Claret (2004). Note that we assume circular orbits for the short-period planets under consideration. We estimate the mass, radius, and surface temperature of each star using the best-fit YREC isochrone (An et al. 2007; also see Paper I), we then estimate the limb-darkening coefficients for each star via linear interpolation within the Claret (2004) grid, assuming $[M/H] = 0.045$ (Paper I) and $v_{\rm turb} = 2$ km s^{-1}.

To determine the dependence of $P_{\epsilon,i}$ on the orbital period, we inject the transits in period bins ranging from 0.4 to 5.0 days with a logarithmic step size of 0.022. For each period bin, we inject $N_{\rm trial}$ transits with periods distributed uniformly in logarithm over the bin, random phases and inclinations distributed uniformly in $\cos i$ over the range $0 \leqslant \cos i \leqslant (R_\star + R_p)/a$. Following B06, we estimate that the error in the recovery fraction $f = N_{\rm recover}/N_{\rm trial}$ is given by

$$\sigma_f = \sqrt{f(1-f)/N_{\rm trial}}. \qquad (11)$$

For each period bin, we initially adopt $N_{\rm trial} = 20$ and continue simulating transits until $\sigma_f \leqslant 0.05$ using selection criteria set 1. We conduct simulations for planetary radii of 0.3, 0.35, 0.4, 0.45, 0.5, 0.6, 0.7, 0.8, 0.9, 1.0, 1.5, and $2.0 R_J$.

5.1.2. Calculating $P_{{\rm mem},i}$

To calculate the membership probability for each star, we use the luminosity functions of the cluster and Galactic field along a strip in the $g-r$ and $g-i$ CMDs enclosing the cluster main sequence (see Figure 9; the determination of the luminosity functions is described in Paper I). This gives the membership probability as a function of r-magnitude only. In Figure 10, we show the membership probability as a function of r. Since this method ignores color information in assigning a probability to stars, it tends to give too high a probability to stars lying away from the cluster main sequence and too low a probability to stars lying close to the main sequence. If the transit detection
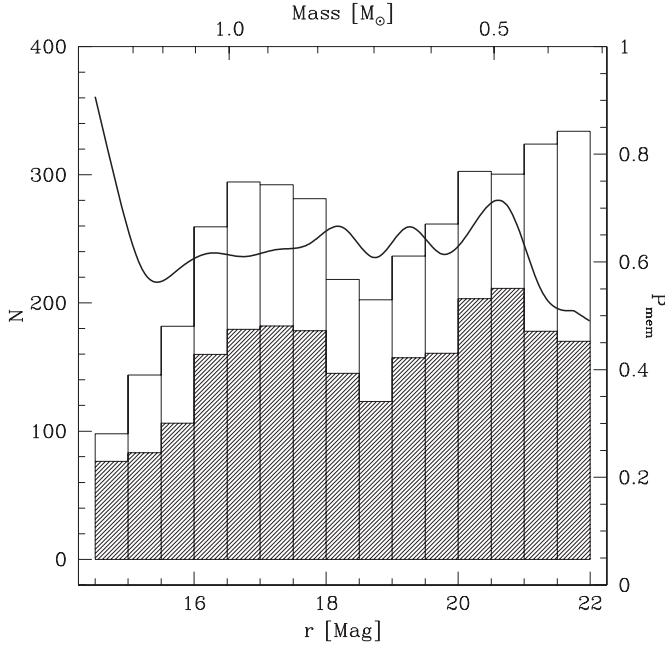
Figure 10. Histogram of stars in the field of the cluster selected in Figure 9 as a function of r-magnitude (open histogram) compared to the histogram of cluster members (filled histogram) taken to be the difference between the histogram of the field on the cluster and the histogram of the field off the cluster. The solid line shows the membership probability (calculated as the ratio of the filled histogram to the open one) as a function of r. The histograms are taken from Paper I and include a correction for photometric incompleteness, but do not correct for spatial incompleteness. This figure is analogous to Figure 9 in B06.

Figure 11. $B-V$ (left) and $V-I_C$ (right) CMDs for stars selected as members of the Galactic field (top), for a simulated observation using the Besançon Galactic models (middle), and for a simulated observation using the Trilegal Galactic model (bottom). For plotting purposes, we have added a Gaussian noise of 0.05 mag to the $V-I_C$ colors from the Besançon model. Stars not selected as cluster members that pass a number of cuts on magnitude, light-curve rms, and the number of points in the light curve (see Section 5.1) are selected as members of the Galactic field. The solid lines show approximately the location of stars selected as potential cluster members; these stars are selected on *gri* CMDs and are not included in the top two CMDs. To estimate the mass and radius for each star in the top two CMDs, we take the values for the nearest star in the middle two CMDs. We use the Trilegal model to estimate the errors in the planet frequency upper limits that result from uncertainties in the Galactic model (Section 6.3). Open stars in the top two plots show points that match to white dwarfs. We reject these stars from our sample.

probability depends only on the r-magnitude of the star, then this simplification should not bias the result. However, as shown in Paper II, cluster members have a higher probability of exhibiting photometric variability than field stars of the same magnitude, so we caution that it is possible that the transit detection probability may be lower on average for cluster members than for field stars. We consider this possibility in Section 6.3.

5.2. Field Stars

To calculate the detection efficiency for field stars, we follow a procedure that is similar to what we use for cluster members. In this case, however, the mass and radius of a star cannot be determined simply from the magnitude of the star. Instead, we use Galactic models to estimate the mass and radius for each star.

First, we select a sample of observed field stars that includes all stars with g, r, i, B, and V photometry that have more than 1000 points in their light curves, have a light-curve rms that is less than 0.1 mag, an instrumental r-band magnitude less than 17 (corresponding roughly to $r \lesssim 22$), and were not selected as candidate cluster members. The sample of stars is shown on $B-V$ and $V-I_C$ CMDs in Figure 11. A total of 7824 stars are selected in this fashion. We then obtain simulated photometric observations of a $24' \times 24'$ field centered at the Galactic latitude/ longitude of the cluster using the Besançon model (Robin et al. 2003). We assume an interstellar extinction of 0.7 mag kpc^{-1}. We caution that this model is known to be unreliable along certain lines of sight (LOSs), in particular for low Galactic latitudes (e.g., see Ibata et al. 2007). For each observed star in our sample, we choose the simulated star that minimizes

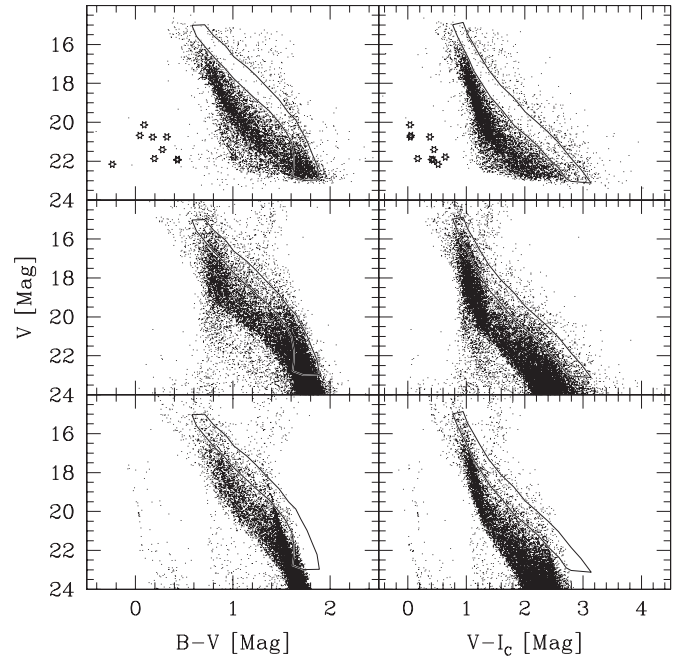$$(V_o - V_s)^2 + (B_o - B_s)^2 + (I_{C,o} - I_{C,s})^2, \qquad (12)$$

where the o subscripts denote photometric measurements for observed stars and the s subscripts denote photometric measurements for simulated stars. We then assign the mass and radius of the simulated star to the observed star. We reject 10 stars that match to white dwarfs since all these lie in an isolated region of the CMD. The majority of the stars in the sample (97%) match to dwarf stars (log $g > 4.0$, cgs) rather than subgiants or giants. Figure 12 shows the estimated radii of the field stars as a function of magnitude compared with the values for the cluster. Note that at fixed magnitude, the majority of field stars have larger radii than the cluster stars. As a result, we expect the transit probability to be larger, but the overall S/N to be smaller at fixed magnitude for the field stars. Thus for signals for which the S/N is much larger than the threshold, the detection efficiency is larger for field stars, but for planets near the S/N threshold, the detection efficiency will be smaller. Thus, the minimum detectable planet radius will be smaller for cluster stars, all else being equal. For the less common foreground field dwarfs, the opposite is true.

We determine the detection efficiency by conducting transit injection and recovery simulations as described in Section 5.1.1. We conduct the simulations for 1000 randomly selected field stars. For each star, we calculate $P_{det,i}$ using Equation (10) where we now take $P_{mem,i} = 1$. The 95% upper limit on the occurrence frequency, assuming no detections, can then be calculated using Equation (9) with the sum in the dominator being multiplied
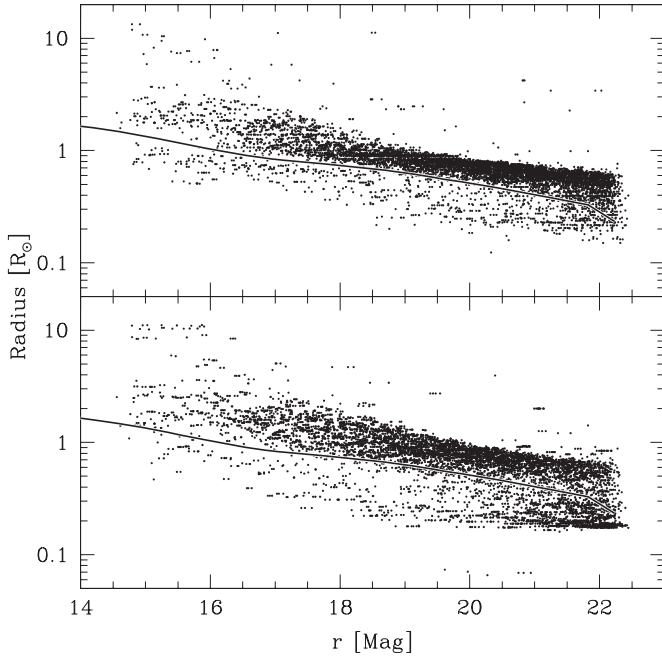
Figure 12. Estimated stellar radius is plotted against the magnitude for Galactic field stars (solid points) when using the Besançon Galactic model (top) and the Trilegal model (bottom). The solid line shows the relation for the cluster.

by 7814/1000 to scale from the simulated subset to the full sample.

6. RESULTS

In Figure 13, we show several examples of transit-injected light curves recovered in our simulations. Note that 1.5 and $1.0R_J$ planets are easily recovered. Also note that the S/N for $0.4R_J$ planets is similar to that for $\sim 1.0R_J$ planets discovered by the field surveys (see, e.g., Pont et al. 2006).

In Figure 14, we plot the detection probability (Equation (10)) as a function of magnitude for 0.5, 1.0, and $1.5R_J$ simulations on candidate cluster members recovered using selection criteria set 2. We show the results for the EHJ ($0.4 < P < 1.0$ days), the VHJ ($1.0 < P < 3.0$ days), and the HJ ($3.0 < P < 5.0$ days) period ranges. For the HJ period range, we use an upper limit of 5.0 days rather than 9.0 days since we do not attempt to recover planets with periods longer than 5.0 days. For each period range and planet radius, we integrate Equation (10) assuming a uniform probability distribution in $\log P$ and a Dirac-δ function distribution in R, that is,

$$\frac{d^2 p}{dP dR} \propto \delta(R - R_0)/P, \qquad (13)$$

where R_0 is the planet radius under consideration. Note that the detection probability for $1.5R_J$ planets orbiting bright stars ($15.0 \lesssim r \lesssim 20.0$) drops relative to the probability for $1.0R_J$ planets. There are two factors that contribute to this: steps 3–5 of the light-curve processing routines described in Section 3.1 distort the high signal-to-noise transits for these large planets often leading to out-of-transit variations in the processed light curves, and the discrepancy between the limb-darkened transit signal and the box-car model becomes significant for the high signal-to-noise transits. When the light curve processing routines are not used (selection set 3), the drop in the detection probability of large planets is less significant; however, the sensitivity to smaller planets is reduced.
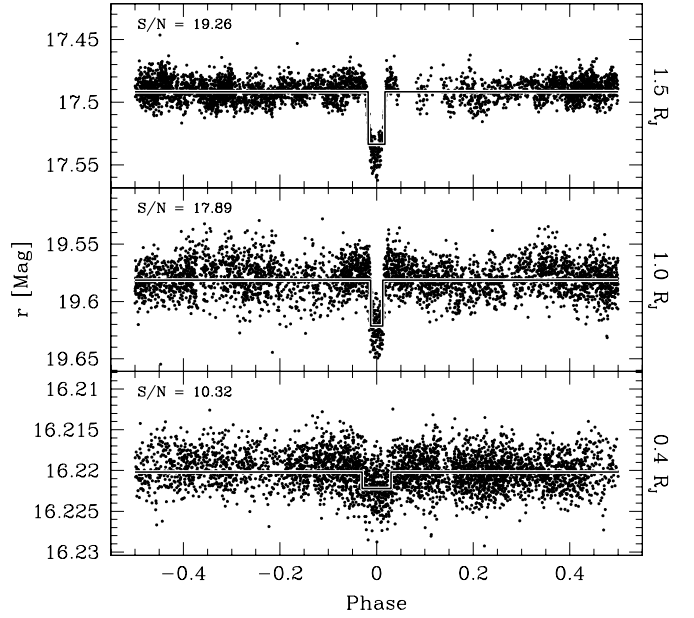

Figure 13. Example-phased light curves of simulated transits that are successfully recovered using selection criteria set 2 (Section 3.2.2). The simulated planets have radii of 1.5, 1.0, and $0.4R_J$ while the stars have radii of 0.70, 0.47, and $0.83R_\odot$, respectively. The injected periods are 1.77, 1.44, and 1.12 days, respectively. The line shows the best-fit box-car transit; we also list the SN for each transit. Note that the examples shown correspond approximately to the median SN recoveries for each planet radius among all recovered simulations with periods between 1.0 and 3.0 days. The 1.5 and $1.0R_J$ planets are easily recovered while the $0.4R_J$ planet is marginally recovered.
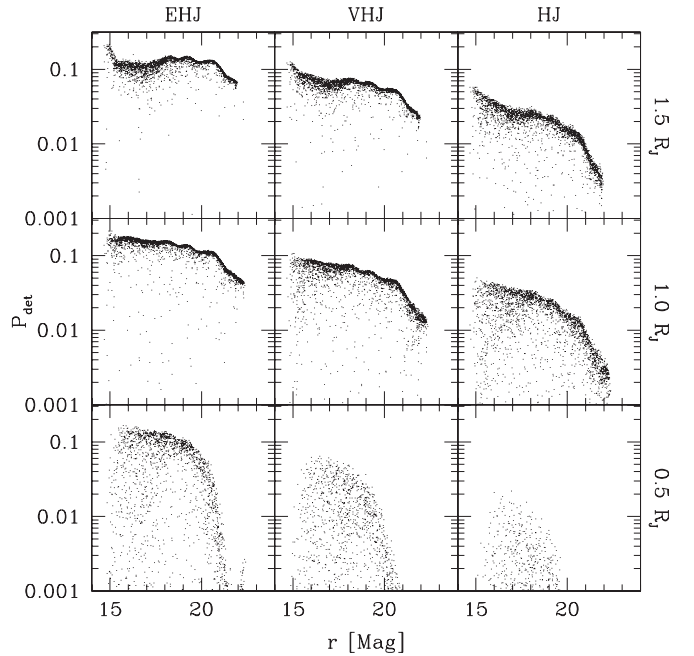

Figure 14. Detection probability as a function of r-magnitude for transit injection/recovery simulations of candidate cluster members. The simulations are recovered using selection criteria set 2. We show the results for the HJ, VHJ, and EHJ period ranges for several planetary radii. The detection probability decreases toward fainter magnitude since the transit probability at fixed period decreases for smaller stars. Note that for very high signal-to-noise transits ($1.5R_J$) the detection probability is lower than expected as a result of the trend-filtering routines.

In Figure 15, we compare the detection probability for field stars to the probability for cluster members; we set $P_{mem} = 1$ for the cluster members in making this comparison. As expected, the
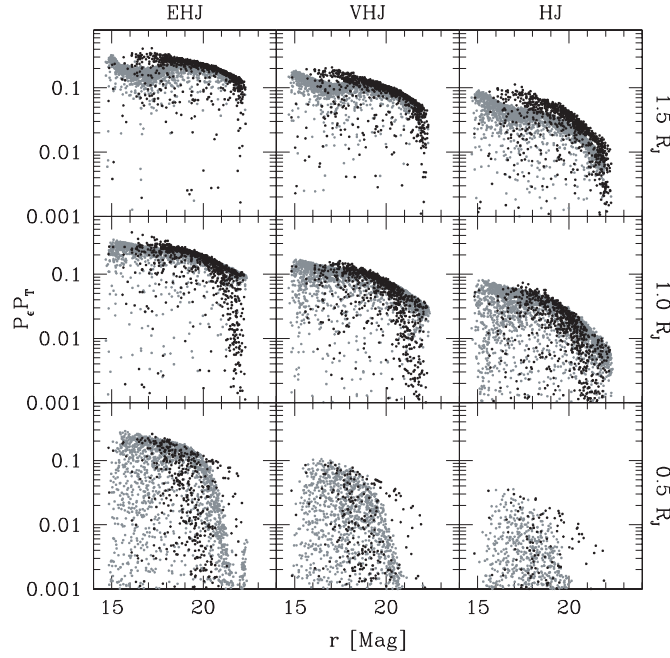
Figure 15. Detection probability as a function of r-magnitude for field stars (dark points) compared with candidate cluster members (light points). We plot $P_\epsilon P_T$, which corresponds to P_{det} when $P_{mem} = 1.0$ for cluster members and is equal to P_{det} for field stars.

Figure 16. $\sim$95% confidence upper limit (solid lines) on the fraction of cluster members (left) and field stars (right) with planets of a given radius as a function of the orbital period. We show the results for 0.35, 0.5, 0.7, and $1.0R_J$ planets. For field stars, we show $0.3R_J$ rather than $0.35R_J$. We also plot the 1σ upper limits (dotted lines) for each of these planet radii.

field stars generally show slightly higher detection probability at fixed magnitude than the cluster members for signals with an S/N well above the detection threshold due to the higher transit probability, but smaller for those signals near the threshold due to the larger radii (and so shallower transits).

Figure 16 shows the $\sim$95% and 1σ confidence upper limits on the planet occurrence frequency for cluster members and field stars as a function of the orbital period using selection criteria set 2. We assume that the orbital periods are uniformly distributed in logarithm within logarithmic period bins of size 0.022 and show the results for several different planet radii. In Figure 17, we show the $\sim$95% confidence upper limits for cluster members as a function of the planet radius for the EHJ, VHJ, and HJ period ranges. We compare the results for the three distinct selection criteria sets. The results are listed in Table 3. We find that the SVM-based selection (selections 2 and 3) outperforms the non-SVM-based selection (selection 1). The upper limits set using SVM are as much as 1.7 times smaller than the upper limits set using the non-SVM selection.

In Figure 18, we show how the distribution of stellar masses to which we are sensitive to planets depends on the planetary radius and period for the cluster candidates and field stars. Note that for $0.3R_J$ planets, the field star distribution is peaked toward smaller stars, whereas the cluster distribution is peaked toward larger stars. The small field stars to which we have sensitivity to $0.3R_J$ planets are foreground stars; at the distance of the cluster, these stars are too faint for us to detect Neptune-sized planets around them. For larger planets, the field star sensitivity distribution is peaked around 0.8–1.0 $M_\odot$, whereas the cluster distribution is broader and peaked at around 0.8 $M_\odot$.

6.1. Cluster Members

For cluster members, we place a 95% confidence upper limit on the frequency of stars with Jupiter-sized EHJ, VHJ, and HJ planets of 1.1%, 2.7%, and 8.3%, respectively. Note that all
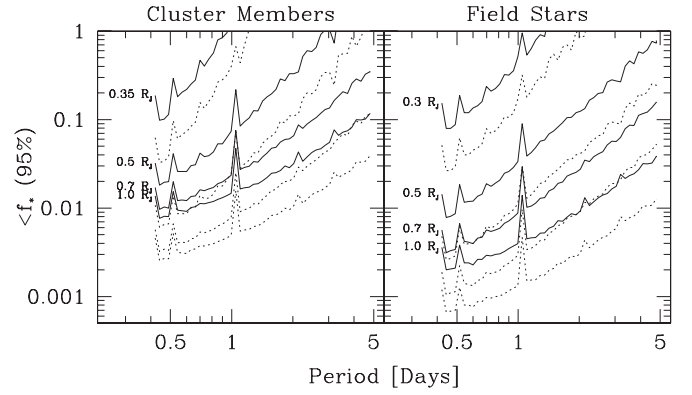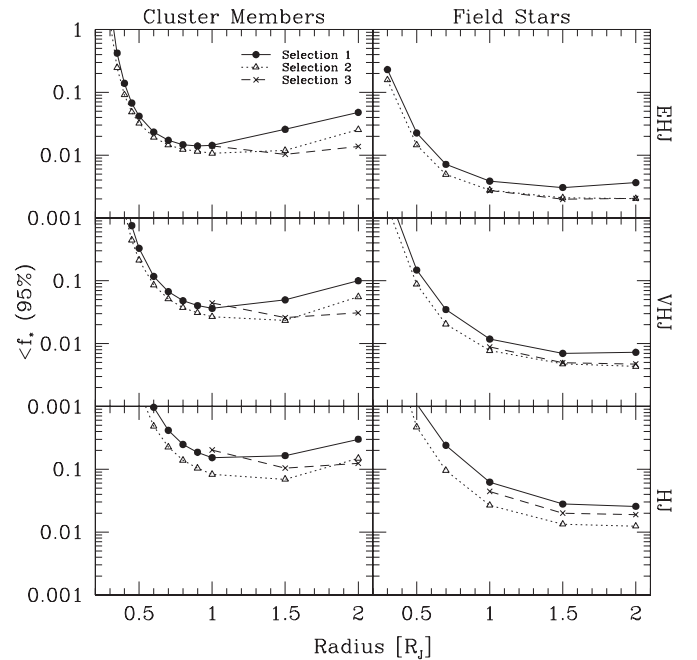

Figure 17. $\sim$95% confidence upper limit on the fraction of cluster members (left) and field stars (right) with planets in a given period range as a function of the planetary radius. We show the results for the EHJ ($0.4 < P < 1.0$ days), VHJ, ($1.0 < P < 3.0$ days), and HJ ($3.0 < P < 5.0$ days) ranges. We compare the results for each of the selection criteria sets discussed in Section 3.2.

of these limits, as well as those we discuss below, come from selection criteria set 2. For smaller planets, the limits rise. For the EHJ period range, we can place a limit of 25% on planets down to $0.35R_J$, which is roughly the size of Neptune. For the VHJ period range, we can place a limit of 44% on planets down to $0.45R_J$, while for the HJ period range, we can place a limit of 49% on planets down to $0.6R_J$.

6.2. Field Stars

The sample of field stars provides more stringent upper limits on the planet occurrence frequency than the sample of cluster members. For this sample we can place a 95% confidence upper limit on the frequency of stars with Jupiter-sized EHJ, VHJ, and HJ planets of 0.3%, 0.8%, and 2.7% respectively. This assumes that the candidate 70127 is not a real planet; if 70127 is real, the frequency of $\sim 1.0R_J$ planets in the EHJ period range would

Table 3
95% Upper Limits on the Planet Occurrence Frequency

|	Period	Selection	$0.3R_J$	$0.35R_J$	$0.4R_J$	$0.45R_J$	$0.5R_J$	$0.6R_J$	$0.7R_J$	$0.8R_J$	$0.9R_J$	$1.0R_J$	$1.5R_J$	$2.0R_J$
Cluster	EHJ	1	1.000	0.421	0.139	0.067	0.042	0.023	0.017	0.015	0.014	0.014	0.026	0.048
		2	1.000	0.247	0.091	0.049	0.032	0.019	0.015	0.012	0.011	0.011	0.012	0.025
		3	⋯	⋯	⋯	⋯	⋯	⋯	⋯	⋯	⋯	0.014	0.010	0.014
	VHJ	1	1.000	1.000	1.000	0.754	0.328	0.117	0.067	0.048	0.040	0.036	0.050	0.100
		2	1.000	1.000	1.000	0.444	0.213	0.086	0.051	0.037	0.031	0.027	0.023	0.056
		3	⋯	⋯	⋯	⋯	⋯	⋯	⋯	⋯	⋯	0.044	0.026	0.031
	HJ	1	1.000	1.000	1.000	1.000	1.000	0.967	0.416	0.248	0.186	0.153	0.165	0.300
		2	1.000	1.000	1.000	1.000	1.000	0.485	0.226	0.139	0.104	0.083	0.069	0.149
		3	⋯	⋯	⋯	⋯	⋯	⋯	⋯	⋯	⋯	0.202	0.104	0.124
Field	EHJ	1	0.230	⋯	⋯	⋯	0.023	⋯	0.007	⋯	⋯	0.004	0.003	0.004
		2	0.158	⋯	⋯	⋯	0.014	⋯	0.005	⋯	⋯	0.003	0.002	0.002
		3	⋯	⋯	⋯	⋯	⋯	⋯	⋯	⋯	⋯	0.003	0.002	0.002
	VHJ	1	1.000	⋯	⋯	⋯	0.148	⋯	0.035	⋯	⋯	0.012	0.007	0.007
		2	1.000	⋯	⋯	⋯	0.088	⋯	0.020	⋯	⋯	0.008	0.005	0.004
		3	⋯	⋯	⋯	⋯	⋯	⋯	⋯	⋯	⋯	0.009	0.005	0.005
	HJ	1	1.000	⋯	⋯	⋯	1.000	⋯	0.240	⋯	⋯	0.062	0.028	0.026
		2	1.000	⋯	⋯	⋯	0.469	⋯	0.095	⋯	⋯	0.027	0.013	0.012
		3	⋯	⋯	⋯	⋯	⋯	⋯	⋯	⋯	⋯	0.044	0.020	0.019
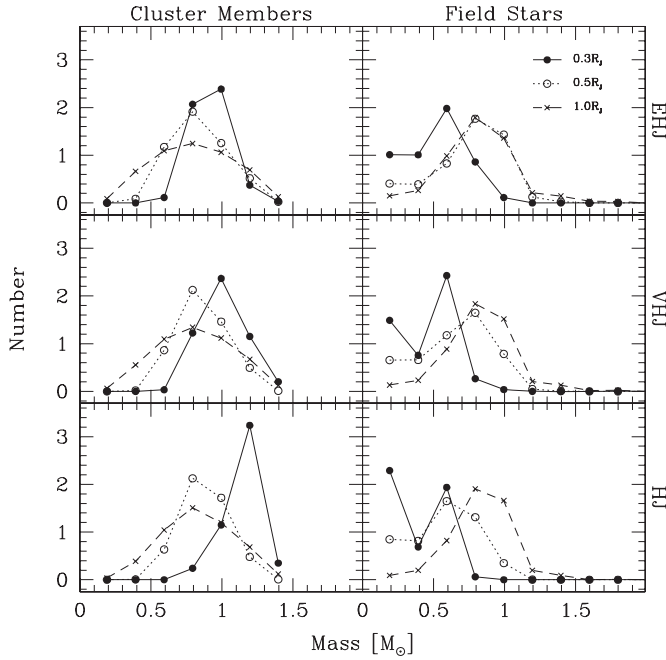
Figure 18. P_{det}-weighted distribution of stellar masses to which we have sensitivity to detect planets. The curves have been normalized to have a unit integral over the range $0.09\ M_\odot < M < 2.1\ M_\odot$. The distributions are plotted for different planetary radii and period ranges, and are shown for cluster candidates (left) and field stars (right) separately. Note that for $0.3R_J$ planets, the field star distribution is peaked toward smaller stars, whereas the cluster distribution is peaked toward larger stars. The small field stars to which we have sensitivity to $0.3R_J$ planets are foreground stars; at the distance of the cluster, these stars are too faint for us to detect Neptune-sized planets around them. For larger planets, the field star sensitivity distribution is peaked at around 0.8–1.0 $M_\odot$, whereas the cluster distribution is broader, but also peaked at around 0.8 $M_\odot$.

Figure 19. Masses and radii of solar system objects (filled circles) and transiting planets (open circles) are compared with two simple mass–radius relations that we adopt for estimating the expected planet yield. The solid line is a power law of the form $R/R_J = 1.5(M/M_J)^{0.5}$ for $M < M_J$ and $R = 1.5R_J$ for $M \geqslant M_J$, the dotted line is a power law of the form $R/R_J = 1.0(M/M_J)^{0.38}$ for $M < M_J$ and $R = R_J$ for $M \geqslant M_J$. The transiting planet data were taken from Torres et al. (2008). For comparison we also show theoretical mass-radius relations for a pure ice planet (dashed line), a gas giant with a $25M_\oplus$ core (long dashed line), and a pure gas giant (dot-dashed line) from Fortney et al. (2007). The gas giant–planet relations are for a planetary semimajor axis of 0.045 AU.

be $0.002\% < f < 0.5\%$ with 95% confidence. In principle, this frequency is small enough that planets in this period range could have escaped detection in most other RV and transit surveys. Some transit surveys have probed enough stars to be sensitive to planets with these frequencies, as some of them have looked at as many or more stars than we have, but these surveys have generally not been very sensitive to hosts with masses as small
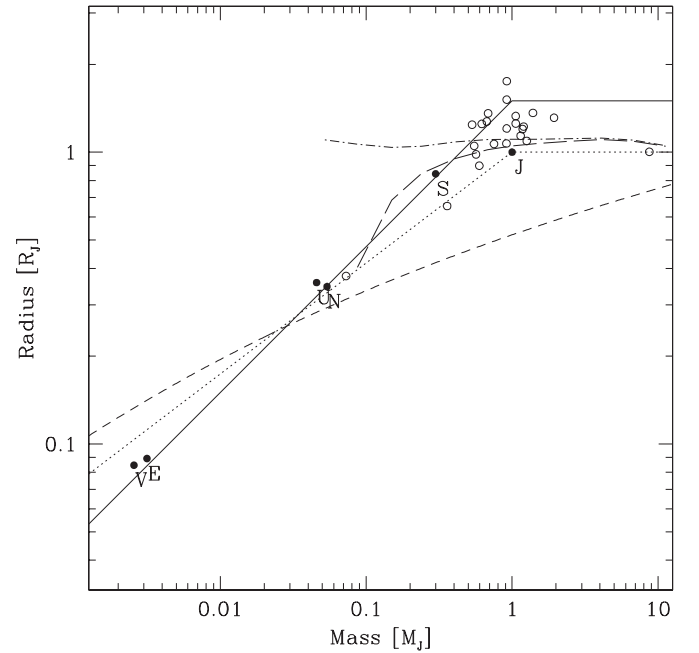
as this host (see Gould et al. 2006; Beatty & Gaudi 2008). For the EHJ period range, we can place a limit of 16% on planets down to $0.3R_J$; for the VHJ range, a limit of 8.8% on planets down to $0.5R_J$; and for the HJ range, a limit of 47% on planets down to $0.5R_J$. Extrapolating the curves in Figure 17, we note that for the EHJ period range, we do have some sensitivity even to planets as small as $\sim2.5R_\oplus$.

Table 4
95% Upper Limits on the Planet Occurrence Frequency for Field Stars Using Different Galactic Models

	Radius [R_J]	EHJ[a]	VHJ	HJ
Trilegal model	0.3	0.143	⋯	⋯
	0.5	0.014	0.082	0.401
	0.7	0.005	0.022	0.104
	1.0	0.003	0.009	0.033
	1.5	0.002	0.005	0.015
	2.0	0.002	0.005	0.013
Besançon model	0.3	0.151	⋯	⋯
$A_V = 0.5$ mag kpc^{-1}	0.5	0.010	0.065	0.394
	0.7	0.004	0.016	0.070
	1.0	0.003	0.007	0.023
	1.5	0.002	0.005	0.014
	2.0	0.002	0.005	0.015

Note. [a] The 95% upper limit on the occurrence frequency of planets with the specified radius and within the EHJ period range.

6.3. Errors on the Upper Limits

There are a number of factors that may contribute errors to the upper limits. This includes uncertainties in P_ϵ from using a finite number of simulations, errors in P_{mem} from using a finite sample, and systematic errors from blends and binaries, from errors in the assumed Galactic model, and from the possibility that cluster members are more likely to be variable than noncluster members. B06 gave a detailed discussion of how most of these errors can be estimated.

The fractional uncertainties in the 95% upper limits for cluster members ($\sigma_{f_{<95\%}}/f_{<95\%}$) due to using a finite number of simulations to determine P_ϵ range from ∼1% for $0.3R_J$ simulations to ∼0.04% for $1.0R_J$ EHJ simulations. For field stars, the fractional uncertainties are all less than 1%. These errors are negligible compared to other sources of uncertainty.

Following B06, we note that the fractional uncertainty in the 95% upper limit for candidate cluster members due to uncertainties in P_{mem} is equal to the fractional uncertainty in the effective number of cluster members: $\sigma_{N_{\star,\mathrm{eff}}}/N_{\star,\mathrm{eff}}$, where $N_{\star,\mathrm{eff}} = N_\star \langle P_{\mathrm{mem}} \rangle$. We find $\sigma_{N_{\star,\mathrm{eff}}}/N_{\star,\mathrm{eff}} = 2\%$.

We expect binarity to be a more significant effect than chance alignments. As we noted in Paper II, we expect ∼1 chance alignment within 0.″1 of two point sources brighter than our detection threshold in our entire field. The effect of binarity on a transit survey is not straightforward. While the blending of light from two stars will dilute the transit signal, the primary star will be slightly smaller than what is assumed when injecting transits. Moreover, if the precision of the light curve is good enough that one could still detect the transit for a given planetary radius and primary star radius if the transit were more than a factor of 2 shallower, then such a planet would be detectable orbiting the primary star for any mass ratio and it may also be detectable orbiting the secondary star. In this case the total number of stars to which one is sensitive to planets is greater than estimated when binarity is neglected (see Gould et al. 2006; Beatty & Gaudi 2008, for further discussion about the effects of binarity). Binarity will only affect the detectability of a transit if the mass ratio is high; B06 estimated that the requirement is $q \gtrsim 0.6$, which they argued is true for only ∼11% of dwarf stars when the binary fraction ∼50%. There is an indication that the binary fraction along the main sequence in M37 is closer to 20% (Kalirai & Tosi 2004), which would reduce the number of high-mass ratio binaries to ∼4% assuming that the mass

ratio distribution in the cluster is the same as for the Galactic field.

To estimate how uncertainties in the inferred masses and radii of field stars that results from uncertainties in the Galactic model affect the planetary frequency upper limits, we recompute the upper limits using the Trilegal 1.2 Galactic model (Girardi et al. 2005). We match the sample of field stars to a simulated set of photometric observations generated with the Trilegal model following the same procedure that we used in Section 5.2 to match to the Besançon model. The Trilegal model is shown in Figures 11 and 12 and is generated assuming a local extinction law of 0.7 mag kpc^{-1}. With this model, we find that 96.5% of stars in our field sample have $\log g > 4.0$, which is comparable to the dwarf fraction found with the Besançon model. In Section 5.2, we computed the transit detection probability for a sample of 1000 field stars by conducting transit injection/recovery simulations with stellar masses and radii adopted from the match to the Besançon model. Here, we avoid the expensive task of conducting additional transit injection/recovery simulations by matching stars in the Trilegal-matched sample to appropriate stars in the Besançon-matched sample. We match each star, i, in the Trilegal-matched sample to the star, j, in the Besançon-matched sample that minimizes

$$(0.2\ln(10)(r_i - r_j))^2 + (2(R_i - R_j)/R_i)^2, \quad (14)$$

where r is the r-magnitude of the star and R is its radius. We then set the transit detection probability for star i equal to the probability for star j determined from the simulations. This choice of weighting between magnitude and radius minimizes differences between the expected transit S/N of the two stars. The upper limits on the planet occurrence frequency are then computed with Equation (9). The results using selection criteria 2 are listed in Table 4. We find that the fractional difference in the planet frequency upper limits from the two Galactic models is $\lesssim 10\%$. The Trilegal model yields a systematically lower upper limit for the $0.3R_J$ and $0.5R_J$ planets but a systematically higher upper limit for larger planets. In a similar manner, we recalculate the upper limits using the Besançon model generated with less extinction (0.5 mag kpc^{-1}). In this case we find that the upper limits for planets smaller than $1.0R_J$ are systematically smaller while the upper limits for larger planets are systematically larger. The fractional differences in the upper limits for $0.7R_J$ and smaller planets range from ∼5% to ∼30%, while for larger planets they range from ∼2% to ∼20%. We adopt a fractional uncertainty of ∼10% on the upper limits due to uncertainties in the Galactic model.

To estimate the effect of variability on the upper limits for cluster members, we compute the upper limits under the extreme case where all candidate cluster members that are variable have $P_{\mathrm{mem}} = 1$ and other stars have $P_{\mathrm{mem}} = (N(r)P_{\mathrm{mem},0}(r) - N_{\mathrm{var}}(r))/(N(r) - N_{\mathrm{var}}(r))$, where $P_{\mathrm{mem},0}$ is the value of P_{mem} when variable and nonvariable stars are weighted equally, $N(r)$ is the number of candidate cluster stars in magnitude bin r, and N_{var} is the number of variable candidate cluster stars in magnitude bin r. The resulting 95% upper limits for selection criteria set 2 are given in Table 5. For small radius planets, the effect is significant, so that the upper limit on $0.35R_J$ EHJ planets, for instance, increases to 38% from 25%. For larger planets, the effect of variability is less important; above $1.0R_J$, the fractional increase in the upper limit is less than 10%.

Assuming that binarity and variability only increase the upper limits, the fractional uncertainty on the upper limits for $1.0R_J$ planets orbiting candidate cluster members is

Radius [R_J]	EHJ[a]	VHJ	HJ
0.35	0.381	1.000	1.000
0.40	0.123	1.000	1.000
0.45	0.060	0.633	1.000
0.50	0.037	0.281	1.000
0.60	0.021	0.103	0.636
0.70	0.015	0.058	0.277
0.80	0.013	0.040	0.161
1.00	0.011	0.028	0.090
1.50	0.012	0.024	0.071
2.00	0.022	0.056	0.154

Note. [a] The 95% upper limit on the occurrence frequency of planets with the specified radius and within the EHJ period range.

$\sim +11\%, -2\%$, and for $0.35R_J$ planets, it is $\sim +50\%, -2\%$. For field stars, we can neglect the uncertainty due to variability and the uncertainty on the membership probability, but we must include the uncertainty on the Galactic model, so that the fractional uncertainty on the upper limit for all planetary radii is $\sim +15\%, -10\%$.

6.4. Comparison with Previous Results

Our results can be compared with both previous results for transit surveys of open clusters and results from transit and RV surveys of the Galactic field.

Our limits of 1.2%, 2.3%, and 6.9% for the cluster on the frequency of EHJ, VHJ, and HJ planets, respectively, with $R = 1.5R_J$ are substantially better than the corresponding limits of 1.5%, 6.4%, and 52% for NGC 1245 by B06. The primary differences between the two surveys are that we observed approximately twice as many cluster members as B06 and we obtained significantly higher precision photometry at fixed stellar radius than B06. Note, however, that B06 used a period range of 3–9 days for the HJ range, whereas we use a range of 3–5 days. Since, by selection, we have zero sensitivity to planets with 5 days $< P <$ 9 days, extending our HJ range to the B06 range results in a limit of $\sim$15% on the fraction of stars with planets of radius $1.5R_J$ (assuming an underlying distribution in P that is uniform in logarithm). Miller et al. (2008) have also conducted detailed Monte Carlo simulations of their open cluster transit survey and placed 95% upper limits of 14% and 45% on a VHJ and HJ, respectively, with radii of $1.5R_J$.

We can estimate the frequency of planets detected by RV surveys in the EHJ, VHJ, and HJ period ranges using the results from Cumming et al. (2008, see Figure 5 in their paper). Out of their sample of 585 FGKM stars, there are seven planets with $M > 0.1M_J$ and 3 days $< P <$ 5 days, one planet with $M > 0.1M_J$ and 1 day $< P <$ 3 days, and no planets detected with $P < 1$ day. This yields 95% confidence intervals for the occurrence frequencies of $0.48\% < f_{HJ} < 2.5\%$, $0.0043\% < f_{VHJ} < 0.95\%$, and $f_{EHJ} < 0.51\%$. Our results are not directly comparable with the RV survey results for two reasons: first, our limits are based on planetary radius while the RV survey limits are based on planetary mass; second, the distribution of stellar masses and metallicities is not the same for the two surveys. Nonetheless, if we assume that all extrasolar giant planets have radii of $\sim 1.0R_J$ and that the planet occurrence

frequency does not depend on stellar properties, then our upper limits of $f_{EHJ} < 0.3\%$, $f_{VHJ} < 0.8\%$, and $f_{HJ} < 2.7\%$ for field stars are consistent with the measured RV frequencies.

Gould et al. (2006) used the results of the OGLE transit survey to determine the frequency of VHJ and HJ planets. Assuming that planets follow a uniform distribution in radius between $1.0R_J$ and $1.25R_J$, they found $f_{VHJ} = 0.14^{+0.19}_{-.08}\%$ and $f_{HJ} = 0.31^{+0.35}_{-0.17}\%$ with 90% confidence error bars. Furthermore, they placed a 95% confidence upper limit of less than 1.7% on planets with periods between one and five days and radii distributed uniformly between 0.78 and $0.97R_J$. Similarly, Fressin et al. (2007) found $f_{VHJ} = 0.18\%$ and $f_{HJ} = 0.29\%$ for the OGLE survey, and they found that the fraction of stars bearing planets with periods less than two days is $0.079^{+0.066}_{-0.040}\%$ with 90% confidence error bars. Note that the frequency of an HJ is lower for the OGLE survey than for the RV surveys because the RV surveys tend to be biased toward higher metallicity stars whereas the OGLE survey is not. Our upper limits on the VHJ and HJ occurrence frequencies for field stars are consistent with the frequencies determined by both of these groups.

We can also compare our results with the results from the SWEEPS survey. Sahu et al. (2006) found that $\sim 0.4^{+0.4}_{-0.2}\%$ of stars larger than $0.44\ M_\odot$ host a Jupiter-sized planet with $P < 4.2$ days, assuming that all 16 of their candidates are real, which is consistent with the limits that we set. Focusing specifically on the EHJ period range, we note that Sahu et al. (2006) found five candidate planets in this range and estimated that at least ~ 2 of them are likely to be real. Assuming that all 16 candidates are real planets, and that 5 of them are an EHJ, their results suggested that $\sim 0.13\%$ of stars host an EHJ. If, on the other hand, we estimate that only half of the candidates are real, and that two of them are an EHJ, the frequency of an EHJ would be $\sim 0.05\%$. Note that we have assumed that the detection probability is constant over the entire period range. Accounting for the enhanced probability of detecting an EHJ over a VHJ and HJ may lower the frequency estimates of these planets by as much as a factor of ~ 5. The SWEEPS frequency of an EHJ is below the 95% upper limit that we set assuming that 70127 is not a real candidate. If 70127 is real, our EHJ frequency of $0.09^{+0.2}_{-0.077}\%$ (with 1σ errorbars) would be consistent with the SWEEPS results.

6.5. Expected Planet Yield

Based on the planet distribution determined by other surveys, we can estimate the expected yield of our survey. Cumming et al. (2008) found that the distribution of planet masses down to $\sim 0.1M_J$ is given by

$$\frac{d^2N}{d\ln M d\ln P} = CM^\alpha P^\beta, \qquad (15)$$

where $\alpha = -0.31 \pm 0.2$ and $\beta = 0.26 \pm 0.1$, M is in Jupiter masses, P is in days, and C is a constant. For notational simplicity, in the following discussion, we do not write factors of M_J and R_J. We will adopt the mass dependence from this relation, but not the period dependence, since this relation does not account for the pile-up of planets at short periods. For the period dependence we adopt a constant $C_{\bar{P}}$ that is appropriate for each period range $\bar{P}$ (i.e., EHJ, VHJ, or HJ). The model distribution is then given by

$$\frac{dN_{\bar{P}}}{d\ln M} = C_{\bar{P}}M^\alpha, \qquad (16)$$

where

$$C_{\bar{P}} = \frac{f_{\bar{P}}\alpha}{M_{\max}^{\alpha} - M_{\min}^{\alpha}}, \qquad (17)$$

and $f_{\bar{P}}$ is the fraction of stars with planets in period range $\bar{P}$ with masses between $M_{\min} = 0.1$ and $M_{\max} = 10$.

We assume a simple planetary mass–radius relation of the form

$$R(M) = \begin{cases} R_0 M^{\gamma}, & M < 1.0 \\ R_0, & M \geqslant 1.0 \end{cases}, \qquad (18)$$

with $\gamma = 0.5$, $R_0 = 1.5$, or $\gamma = 0.38$, $R_0 = 1$ (see Figure 19). We consider two different mass-radius relations to determine the sensitivity of our results to the assumed relation. The expected number of planet detections in the EHJ, VHJ, and HJ period ranges is then given by

$$N_{\bar{P}} = \sum_i \left(\int_{R_{\min}}^{R_0} \gamma^{-1} C_{\bar{P}} \left(\frac{R}{R_0} \right)^{\alpha/\gamma} R^{-1} P_{\det,\bar{P},i}(R) dR \right.$$
$$\left. + P_{\det,\bar{P},i}(R_0) C_{\bar{P}} \alpha^{-1} \left(M_{\max}^{\alpha} - 1 \right) \right), \qquad (19)$$

where the sum is over all stars in the sample, $P_{\det,\bar{P},i}(R)$ is the planet detection probability for star i for planets with radii R restricted to the period range $\bar{P}$, and $R_{\min}$ is a minimum planetary radius below which $P_{\det} = 0$ for all stars (we take $R_{\min} = 0.3$). Note that we assume that the planetary mass and period distribution are independent of the stellar mass.

We expect that the sample of stars surveyed by the RV planet searches, which is biased toward high metallicity, provides a better match to the metallicity of the cluster than the stars surveyed by the OGLE transit search, whereas the OGLE sample provides a better match to the metallicity of the field stars than the RV sample. We therefore use the frequencies of the HJ and VHJ planets from Cumming et al. (2008) for the cluster and the frequencies from Gould et al. (2006) for the field. We take the frequency of an EHJ inferred from the SWEEPS survey for both the field and the cluster. Fixing C_{HJ}, C_{VHJ}, and C_{EHJ} for cluster members such that the fraction of stars with an HJ, VHJ, and EHJ larger than 0.1 $M_{\odot}$ is 0.012, 0.0017, and 0.0005, respectively, we find $C_{\mathrm{HJ}} = 2.4 \times 10^{-3}$, $C_{\mathrm{VHJ}} = 3.4 \times 10^{-4}$ and $C_{\mathrm{EHJ}} = 1.0 \times 10^{-4}$. For the field stars, we use the frequencies from Gould et al. (2006) to set $C_{\mathrm{HJ}} = 6.2 \times 10^{-4}$ and $C_{\mathrm{VHJ}} = 2.8 \times 10^{-4}$.

Using the above model and $P_{\det}(R)$ values from selection criteria set 2, we find that for cluster members we would expect to detect ~0.10–0.12 EHJ planets, 0.11–0.16 VHJ planets, and 0.23–0.35 HJ planets where the range depends on the assumed mass-radius relation. For field stars, on the other hand, the expected number of detections are ~0.34–0.51, 0.30–0.54, and 0.18–0.39. We conclude that for the above model, we would have expected to detect ~1.3–2 stars in our entire survey, and therefore our observations are consistent with the model. Finally, we note that Beatty & Gaudi (2008) predicted that there are ~6 transiting HJ and VHJ planets per square degree orbiting Sun-like stars with $V \leqslant 20$ at Galactic latitude $b = 3°.1$ (see Figure 8 of that paper). For our 0.16 deg² survey, they would predict ~1

transiting planet detection, which is comparable to the expected planet yield around field stars from our simulations.

7. DISCUSSION

We have presented the results of a deep ~20 night survey for transiting hot planets in the open cluster M37. This survey stands out from previous ground-based transit surveys both in terms of the size of the telescope used and the photometric precision attained. We observed ~1450 cluster members with masses between $0.3\,M_{\odot} \lesssim M \lesssim 1.3\,M_{\odot}$ as well as 7814 Galactic field stars with masses between $0.1\,M_{\odot} \lesssim M \lesssim 2.1\,M_{\odot}$. While no candidate planets were found among the cluster members, we did identify one candidate EHJ with a period of 0.77 days transiting a Galactic field star. However, the follow-up spectroscopic observations needed to confirm the planetary nature of this candidate would be difficult (although perhaps not impossible) to obtain with current technology, given the faintness of the source. We note that if this candidate is real, then we conclude that $0.09^{+0.2}_{-0.077}\%$ of FGKM stars have Jupiter-sized planets with periods between 0.5 and 1.0 days. This result would be consistent with the results from the SWEEPS survey, and would confirm this new class of ultrashort-period planets. We also note that this planet frequency is small enough that these planets could have escaped detection in most other RV and transit surveys.

The primary result of this survey is an upper limit on the frequency of planets smaller than $1.0R_J$. For cluster members, we find that at 95% confidence less than 25% of stars have planets with radii as small as $0.35R_J$ and periods shorter than one day, less than 44% of stars have planets with radii as small as $0.45R_J$ and periods between 1.0 and 3.0 days, and less than 49% of stars have planets with radii as small as $0.6R_J$ and periods between 3.0 and 5.0 days. The upper limits on the smallest planets may be as much as a factor of 50% higher if all the variable stars near the cluster main sequence are cluster members. For the field stars, we are able to place 95% confidence upper limits of 16% on the fraction of stars with planets as small as $0.3R_J$ with periods less than one day, 8.8% on the fraction of stars with planets as small as $0.5R_J$ with periods between 1.0 and 3.0 days and 47% on the fraction of stars with planets as small as $0.5R_J$ with periods between 3.0 and 5.0 days. We estimate that these upper limits may be higher by at most a factor of ~11% due to binarity. While these limits do not approach the observed frequency of Jupiter-sized planets with similar periods, they do represent the first limits on the frequency of planets as small as Neptune. We can now state empirically that extremely hot Neptunes (periods shorter than one day) are not ubiquitous nor are very hot planets with radii intermediate between Neptune and Saturn.

The limits that we place on Jupiter-sized planets are more stringent than previous open cluster transit surveys, but are still above the frequencies measured by RV and Galactic field transit surveys. The primary limitation on open cluster transit surveys appears to be the paucity of stars in these systems. To place a limit on the frequency of an HJ that is less than 2% with the same set of observations, M37 would have to have been ~4 times richer than it is. We also note that for a relatively young cluster like M37, variability may reduce the detectability of Neptune-sized planets by as much as ~50%.

REFERENCES

Aigrain, S., Hodgkin, S., Irwin, J., Hebb, L., Irwin, M., Favata, F., Moraux, E., & Pont, F. 2007, MNRAS, 375, 29
Alard, C. 2000, A&AS, 144, 363
Alard, C., & Lupton, R. H. 1998, ApJ, 503, 325
Alonso, R., et al. 2004, ApJ, 613, L153
An, D., Terndrup, D. M., Pinsonneault, M. H., Paulson, D. B., Hanson, R. B., & Stauffer, J. R. 2007, ApJ, 655, 233
Bakos, G., et al. 2007, ApJ, 656, 552
Beatty, T. G., & Gaudi, B. S. 2008, ApJ, 686, 1302
Bouchy, F., Pont, F., Santos, N. C., Melo, C., Mayor, M., Queloz, D., & Udry, S. 2004, A&A, 421, L13
Bramich, D. M., et al. 2005, MNRAS, 359, 1096
Brunini, A., & Cionco, R. G. 2005, Icarus, 177, 264
Bruntt, H., Grundahl, F., Tingley, B., Frandsen, S., Stetson, P. B., & Thomson, B. 2003, A&A, 410, 323
Burke, C. J., Gaudi, B. S., DePoy, D. L., & Pogge, R. W. 2006, AJ, 132, 210 (B06)
Butler, P., et al. 2004, ApJ, 617, L580
Butler, R. P., et al. 2006, ApJ, 646, 505
Carraro, G., Villanova, S., Demarque, P., McSwain, M. V., Piotto, G., & Bedin, L. R. 2006, ApJ, 643, 1151
Claret, A. 2004, A&A, 428, 1001
Collier-Cameron, A., et al. 2007, MNRAS, 375, 951
Cumming, A., Butler, R. P., Marcy, G. W., Vogt, S. S., Wright, J. T., & Fischer, D. A. 2008, PASP, 120, 531
Dorren, J. D. 1987, ApJ, 320, 756
Endl, M., Cochran, W., Wittenmyer, R., & Boss, A. 2008, ApJ, 673, 1165
Fischer, D. A., & Valenti, J. 2005, ApJ, 622, 1102
Fischer, D. A., et al. 2008, ApJ, 675, 790
Fortney, J. J., Marley, M. S., & Barnes, J. W. 2007, ApJ, 659, 1661
Fressin, F., Guillot, T., Morello, V., & Pont, F. 2007, A&A, 475, 729
Gaudi, B. S. 2007, in ASP Conf. Ser. 366, Transiting Extrasolar Planets Workshop, ed. C. Alfonso, D. Weldrake, & Th. Henning (San Francisco, CA: ASP), 273
Gaudi, B. S., Seager, S., & Mallén-Ornelas, G. 2005, ApJ, 623, 472
Gilliland, R. L., et al. 2000, ApJ, 545, L47
Gillon, M., et al. 2007, A&A, 472, L13
Girardi, L., Groenewegen, M. A. T., Hatziminaoglou, E., & da Costa, L. 2005, A&A, 436, 895
Gould, A., Dorsher, S., Gaudi, B. S., & Udalski, A. 2006, Acta Astron., 56, 1
Gratton, R., Bragaglia, A., Carretta, E., & Tosi, M. 2006, ApJ, 642, 462
Hartman, J. D., Stanek, K. Z., Gaudi, B. S., Holman, M. J., & McLeod, B. A. 2005, AJ, 130, 2241
Hartman, J. D., et al. 2008a, ApJ, 675, 1257 (Paper I)
Hartman, J. D., et al. 2008b, ApJ, 675, 1233 (Paper II)
Hartman, J. D., et al. 2009, ApJ, 691, 342 (Paper III)
Hood, B., et al. 2005, MNRAS, 360, 791
Ibata, R., Martin, N. F., Irwin, M., Chapman, S., Ferguson, A. M. N., Lewis, G. F., & McConnachie, A. W. 2007, ApJ, 671, 1591
Ida, S., & Lin, D. N. C. 2004, ApJ, 604, 388
Ida, S., & Lin, D. N. C. 2005, ApJ, 626, 1045
Janes, K. 1996, J. Geophys. Res., 101, 14853
Joachims, T. 1999, in Making Large-Scale SVM Learning Practical. Advances in Kernel Methods—Support Vector Learning, ed. B. Schölkopf, C. Burges, & A. Smola (Cambridge, MA: MIT Press)

Joachims, T. 2002, Learning to Classify Text Using Support Vector Machines (Norwell: Kluwer)
Kalirai, J. S., & Tosi, M. 2004, MNRAS, 351, 649
Kalirai, J. S., Bergeron, P., Hansen, B. M. S., Kelson, D. D., Reitzel, D. B., Rich, R. M., & Richer, H. B. 2007, ApJ, 671, 748
Kalirai, J. S., Ventura, P., Richer, H. B., Fahlman, G. G., Durrell, P. R., D'Antona, F., & Marconi, G. 2001, AJ, 122, 3239
Kaluzny, J., & Udalski, A. 1992, Acta Astron., 42, 29
Konacki, M., Torres, G., Jha, S., & Sasselov, D. D. 2003, Nature, 421, 507
Konacki, M., et al. 2004, ApJ, 609, L37
Kovács, G., Bakos, G., & Noyes, R. W. 2005, MNRAS, 356, 557
Kovács, G., Zucker, S., & Mazeh, T. 2002, A&A, 391, 369
Kurtz, M. J., & Mink, D. J. 1998, PASP, 110, 934
Kurucz, R. L. 1993, in IAU Coll. 138, Peculiar versus Normal Phenomena in A-Type and Related Stars, ed. M. M. Dworetsky, F. Castelli, & R. Faraggiana (San Francisco, CA: ASP), 87
Lomb, N. R. 1976, Ap&SS, 39, 447
Lovis, C., et al. 2006, Nature, 441, 305
Mandel, K., & Agol, E. 2002, ApJ, 580, L171
Marcy, G., Butler, R. P., Fischer, D., Vogt, S., Wright, J. T., Tinney, C. G., & Jones, H. R. A. 2005, Prog. Theor. Phys. Suppl., 158, 24
Mayor, M., & Queloz, D. 1995, Nature, 378, 355
McCullough, P., et al. 2006, ApJ, 648, 1228
McLeod, B. A., Conroy, M., Gauron, T. M., Geary, J. C., & Ordway, M. P. 2000, in Proc. Int. Conf. on Scientific Optical Imaging, Further Developments in Scientific Optical Imaging, ed. M. Bonner Denton (Cambridge: Royal Society of Chemistry), 11
Melo, C., et al. 2007, A&A, 467, 721
Miller, A. A., Irwin, J., Aigrain, S., Hodgkin, S., & Hebb, L. 2008, MNRAS, 387, 349
Mochejska, B. J., et al. 2005, AJ, 129, 2856
Mochejska, B. J., et al. 2006, AJ, 131, 1090
Montalto, M., et al. 2007, A&A, 470, 1137
Nilakshi Sagar, R. 2002, A&A, 381, 65
Origlia, L., Valenti, E., Rich, R. M., & Ferraro, F. R. 2006, ApJ, 646, 499
Pepper, J., & Gaudi, B. S. 2005, ApJ, 631, 581
Pepper, J., & Gaudi, B. S. 2006, Acta Astron., 56, 183
Pont, F., Bouchy, F., Queloz, D., Santos, N., Melo, C., Mayor, M., & Udry, S. 2004, A&A, 426, L15
Pont, F., Zucker, S., & Queloz, D. 2006, MNRAS, 373, 231
Press, W. H., & Rybicki, G. G. 1989, ApJ, 338, 277
Press, W. H., Teukolsky, S. A., Vetterling, W. T., & Flannery, B. P. 2007, in Numerical Recipes: The Art of Scientific Computing (3rd ed.; New York: Cambridge Univ. Press)
Rivera, E., et al. 2005, ApJ, 634, 625
Robin, A. C., Reylé, C., Derrière, S., & Picaud, S. 2003, A&A, 409, 523
Sahu, K., et al. 2006, Nature, 443, 534
Santos, N., et al. 2004, A&A, 426, L19
Scargle, J. D. 1982, ApJ, 263, 835
Skrutskie, M. F., et al. 2006, AJ, 131, 1163
Stetson, P. B. 1987, PASP, 99, 191
Stetson, P. B. 1990, PASP, 102, 932
Stetson, P. B. 1992, JRASC, 86, 71
Stetson, P. B., Bruntt, H., & Grundahl, F. 2003, PASP, 115, 413
Street, R. A., et al. 2003, MNRAS, 340, 1287
Szentgyorgyi, A. H., Cheimets, P., Eng, R., Fabricant, D. G., Geary, J. C., Hartmann, L., Pieri, M. R., & Roll, J. B. 1998, in Proc. SPIE 3355, Optical Astronomical Instrumentation, ed. S. D'Odorico (Bellingham, WA: SPIE), 242
Tingley, B., & Sackett, P. D. 2005, ApJ, 627, 1011
Torres, G., Winn, J. N., & Holman, M. J. 2008, ApJ, 677, 1324
Udalski, A., et al. 2002, Acta Astron., 52, 1
Udry, S., et al. 2006, A&A, 447, 361
Udry, S., et al. 2007, A&A, 469, L43
Vapnik, V. N. 1995, The Nature of Statistical Learning Theory (New York: Springer)
Vogt, S., et al. 2005, ApJ, 632, 638
von Braun, K., Lee, B. L., Seager, S., Yee, H. K. C., Mallén-Ornelas, G., & Gladders, M. D. 2005, PASP, 117, 14
Weldrake, D. T. F., Sackett, P. D., & Bridges, T. J. 2008, ApJ, 674, 1117
Weldrake, D. T. F., Sackett, P. D., Bridges, T. J., & Freeman, K. C. 2005, ApJ, 620, 1043